

Transient and asymptotic kinetics of mass transfer by coupled surface and grain boundary diffusion in sintering under strain rate control

Francis Delannay^{a*} and Laurence Brassart^b

^a Université catholique de Louvain, Institute of Mechanics, Materials and Civil Engineering, iMMC/IMAP, Place Sainte Barbe 2, B-1348 Louvain-la-Neuve, Belgium francis.delannay@uclouvain.be.

^b Monash University, Department of Materials Science and Engineering, Clayton, VIC 3800, Australia
laurence.brassart@monash.edu

Abstract

An original procedure is developed for simulating pore surface evolution during sintering at high strain rate while distinguishing two types of diffusion fluxes: transient surface fluxes governed by short range curvature gradients, and coupled fluxes at surface and grain boundary governed by strain-rate. The latter fluxes become dominant asymptotically, i.e. after damping-out of transient fluxes. The procedure aims at allowing the prediction of the strain rate dependence of macroscopic viscosity, a concept which is meaningful only during the asymptotic stage. The problem is addressed in 2D. It is shown that the asymptotic solution of the general partial differential equation of the problem can be obtained as the solution of an ordinary differential equation, of which the resolution lends itself to a semi-analytical procedure. An estimate is also proposed for the rate of convergence of the general solution towards the asymptotic solution. The accuracy of the mathematical procedure is validated by a comparison of the evolution of asymptotic profiles and exact profiles calculated fully numerically during densification or expansion of the system. A method is proposed for mapping the conditions of existence of an asymptotic stage. The method can account for the dependence of average grain coordination on relative density.

Keywords : sintering, diffusion, viscosity, grain coordination

* Corresponding author: francis.delannay@uclouvain.be. Tél +32479738784

1. Introduction

It is widely admitted that, under usual conditions of temperature and loading (excluding hot forging), the sintering rheology of crystalline materials with grain size smaller than $\sim 50 \mu\text{m}$ is governed by the coupling of diffusion along pore surfaces and along grain boundaries [1]. As sketched in Fig. 1, two types of diffusion fluxes on pore surfaces can then be distinguished:

- A. the diffusion fluxes (denoted j_{sA}) feeding the reversible exchange of matter between grain boundaries and pore surface: these fluxes are driven by sintering stress and external loading and bring about macroscopic straining, i.e. densification or expansion, possibly coupled with shear;
- B. the diffusion fluxes (denoted j_{sB}) feeding the transient, irreversible transfer of matter from surface to surface: these fluxes are driven by curvature gradients having a characteristic length smaller than grain size; they do not bring about macroscopic straining.

Following Coble [2, 3], three stages of sintering are commonly distinguished. During initial and intermediate stages, pore volume is considered to be fully continuous whereas it is considered discontinuous during the final stage. Beside this difference in pore volume topology, the distinction between the initial stage and the intermediate/final stages stems from the nature of the dominant surface diffusion fluxes. The initial stage is defined as the stage during which transient fluxes of type j_{sB} are dominant. Its kinetics is a function of microstructural parameters (grain size, grain coordination, relative density) and material parameters (surface tension, surface diffusivity) and is not linked to macroscopic strain rate $\dot{\epsilon}$. This means that the system evolution entirely belongs to the initial stage if external loading prevents densification. Intermediate and final stages are governed by fluxes of type j_{sA} . These fluxes dominate when

fluxes of type j_{sB} have sufficiently damped out: intermediate and final stages thus belong to the asymptotic behaviour of the system. Their kinetics is linked to macroscopic strain rate $\dot{\epsilon}$. Curvature gradients driving diffusion at pore surface then have a characteristic length that scales with pore size and amplitude that scales with strain rate. In principle, $\dot{\epsilon}$ can be controlled by proper control of the external loading setup.

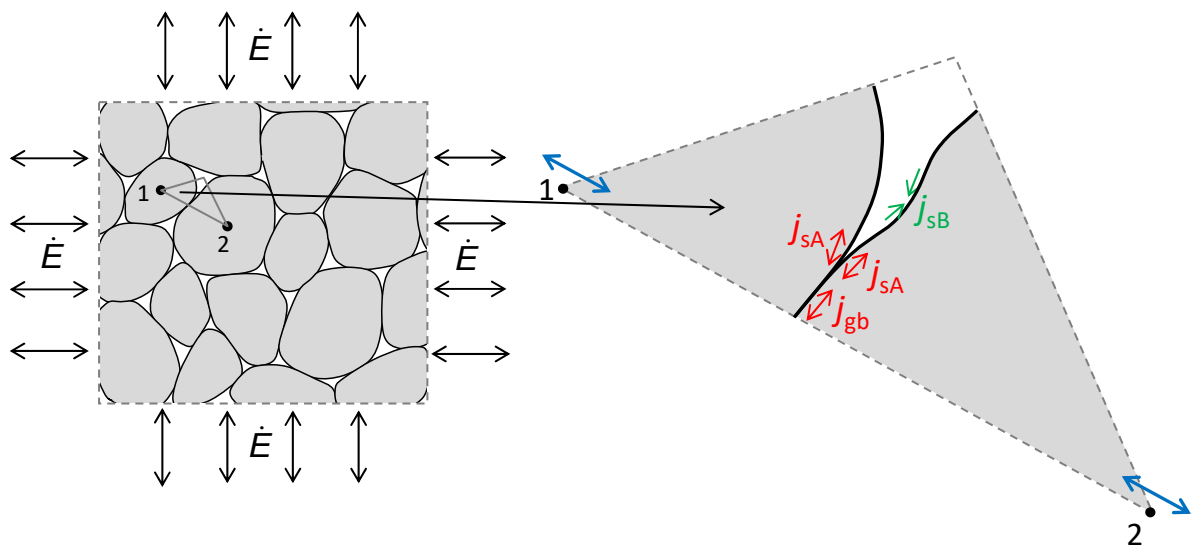


Figure 1: Two types of surface diffusion fluxes: fluxes j_{sA} (red) feed grain boundary diffusion fluxes j_{gb} , the divergence of which brings about relative displacement of the centroids of grains 1 and 2; fluxes j_{sB} (green) are driven by small scale curvature gradient and are not coupled to macroscopic strain rate.

Constitutive laws for numerical simulation of sintering processes require the input of a macroscopic viscosity tensor which, for an isotropic body, reduces to only two scalar parameters commonly called bulk viscosity and shear viscosity. Ideally, these macroscopic parameters should be obtained by modelling dissipative phenomena arising at grain scale and pore scale in such a way as to explicitly account for the relevant microstructural and material parameters as well as for the strain rate. Much effort has been invested in literature to develop

such models for the intermediate and final stages of sintering [4-11] (obviously, the concept of sintering viscosity is meaningful only provided the asymptotic behaviour dominates the overall evolution of the system). The large majority of these models rely on the so-called “quasi-equilibrium approximation”, which consists in neglecting the effect of surface diffusion during the intermediate and final stages. This amounts to neglecting curvature gradients, i.e. to considering that, during these two stages, pore shape remains undistinguishable from the static equilibrium shape with uniform curvature. As the ratio $\Delta = \frac{\delta D_{gb}}{\delta D_s}$ of grain boundary diffusivity to surface diffusivity increases with homologous temperature (up to reach $\Delta \approx 1$ at the melting point), the quasi-equilibrium approximation is commonly considered to be valid in usual sintering conditions as long as homologous temperature is not too high. Models based on the quasi-equilibrium approximation predict a Newtonian viscosity, i. e. a viscosity independent of strain rate. The quasi-equilibrium approximation is implicit in current finite element codes resting on linearly viscous constitutive laws [12].

As the amplitude of curvature gradients increases when macroscopic strain rate increases, the validity of the quasi-equilibrium approximation breaks down at the high strain rates used in the various fast sintering methods which are becoming increasingly practiced nowadays [13-17]. Moreover, the classical distinction between sintering stages can then become questionable: no distinction between initial and intermediate stages can still be made if full density is reached before transient transfers of matter from surface to surface have damped out. The final objective of our work is to improve microstructural models in order to allow predicting the strain rate dependence of macroscopic viscosity at the high strain rates used in fast sintering methods. This means that, during the asymptotic stage, the contribution of surface diffusion to

dissipation cannot be neglected *a priori* with respect to the contribution of grain boundary diffusion. Macroscopic rheology can then become non-Newtonian. No comprehensive physics-based modelling of macroscopic rheology not resting on the quasi-equilibrium approximation has been proposed yet in literature.

Previous studies in literature have addressed by numerical methods the simulation of pore surface evolution during sintering by coupled surface and grain boundary diffusion. 3D models have essentially been limited to the analysis of the evolution of the neck at the point of contact between two spheres and the subsequent merging of the spheres during free sintering [18-22]. The evolution of the pore architecture inside a packed aggregate has been analysed only via 2D models. Hsueh and Evans [23], Riedel [24] and Mullins [25, 26] used the quasi-equilibrium approximation for describing the evolution of the (uniform) pore curvature during free sintering of a hexagonal array of cylinders. Mullins proposed in particular a criterion linking pore curvature to the maximum diffusivity ratio Δ beyond which the quasi-equilibrium approximation fails. Subsequently, four papers presented 2D numerical simulations not based on the quasi-equilibrium approximation [27-30]. These papers highlighted the influence of Δ on the time to pore collapse and on the evolution of pore shape and relative density, ρ , during free sintering. In several cases, simulations considered the possibility of Δ values even larger than 1. In the evolution of pore shape, the authors did not attempt to distinguish the contributions of transient and strain-rate-related phenomena and did not elucidate the strain rate dependence of the contribution of surface diffusion on the macroscopic rheology.

In this paper, we develop numerical and semi-analytical methods in 2D for allowing distinction between transient and asymptotic, strain-rate-controlled phenomena when they operate simultaneously during sintering under high imposed strain rate. The methods allow us to

calculate the evolution of pore shape and grain boundary size under purely radial loading in plane strain without resting on the quasi-equilibrium approximation. Model parameters are the macroscopic strain rate \dot{E} (considered to be kept constant by control of external loading), the relative density ρ , the dihedral angle ψ , the average grain coordination Z , and the diffusivity ratio Δ (for which we limit the range to $0 < \Delta < 1$ as we consider that $\Delta > 1$ cannot exist in crystalline materials). The model makes possible the account of the evolution of Z with ρ . In a subsequent paper [31], the methods developed in the present paper will be exploited for computing the strain rate dependence of the contributions of surface diffusion and grain boundary diffusion to the macroscopic bulk sintering viscosity parameter.

The paper contains two main sections. Model and equations are presented in Section 2, which involves three subsections dealing successively with the representative volume element, the full numerical resolution of the partial differential equation (PDE) of the problem expressed in Cartesian coordinates, and the resolution of the PDE expressed in polar coordinates. It is shown that the latter PDE can lead to an asymptotic solution which can be derived via a semi-analytical procedure. A method is proposed for evaluating the damping rate of the transient component of the general solution. The reader is referred to Appendices for the detail of some mathematical developments. Computational results are highlighted and discussed in Section 3. Section 3.1 analyses the rate of convergence of the profiles calculated via the full numerical procedure toward the asymptotic profiles. In Section 3.2, a criterion based on the rates of evolution of transient and asymptotic components is used for delineating, on a map of strain rate versus relative density, regions in which the system evolution is dominated by either of the two phenomena. Practical application in sintering simulation is briefly illustrated in Section 3.3.

2. Model and equations

We consider a bundle of infinitely elongated grains with random transverse isotropy undergoing purely radial densification or expansion (i.e. plane strain deformation). The radial strain rate component, denoted \dot{E} , is negative in the case of densification and positive in the case of expansion (whatever the function A , use is made of the notation \dot{A} for designating either $\frac{dA}{dt}$ or $\frac{\partial A}{\partial t}$). The macroscopic stress tensor is thus also radial in the plane: the in-plane component writes $S_{\infty} = S + \Sigma$ where S is referred to as the viscous stress and Σ is the so-called sintering stress that arises from the thermodynamic forces driving free sintering ($\dot{E} = 0$ and $S = 0$ when $S_{\infty} = \Sigma$).

2.1. Representative volume element for arbitrary average grain coordination

The model represents the system as a bundle of grains having identical size, of which the measure is taken to be the radius R_G of a cylinder of same volume. For illustration, Figure 2 compares arrays of identical grains with $Z = 4$ and 6. Let A be the centre of gravity of a grain, J the middle of a grain boundary, T the triple line, O the centre of gravity of a pore and M the centre of symmetry of the pore profile. If the array undergoes purely radial deformation, the RVE may be limited to the triangle $AJTOM$ in grey shade. This triangle is defined by two parameters: the opening angle

$$\beta = \frac{\pi}{Z}, \quad (1)$$

and the height H , which is related to β , R_G , and ρ as

$$H = \sqrt{\frac{\pi}{Z\rho \tan \beta}} R_G = \sqrt{\frac{\beta}{\rho \tan \beta}} R_G \quad (2)$$

In Fig.2, dihedral angle ψ was taken high enough for the pore curvature to be convex (i.e. for the solid surface to be concave). At static equilibrium, the transition from convex to concave pore curvature occurs for $\beta = \frac{\psi}{2}$. The macroscopic strain rate is

$$\dot{E} = \frac{\dot{H}}{H} \quad (3)$$

From Eq. (2),

$$\frac{\dot{H}}{H} = -\frac{1}{2} \frac{\dot{\rho}}{\rho} \quad (4)$$

In the following, as we restrict ourselves to consider a constant value of \dot{E} , Eqs. (3) and (4) will be used for the conversion between time, t , and relative density, $\rho(t)$.

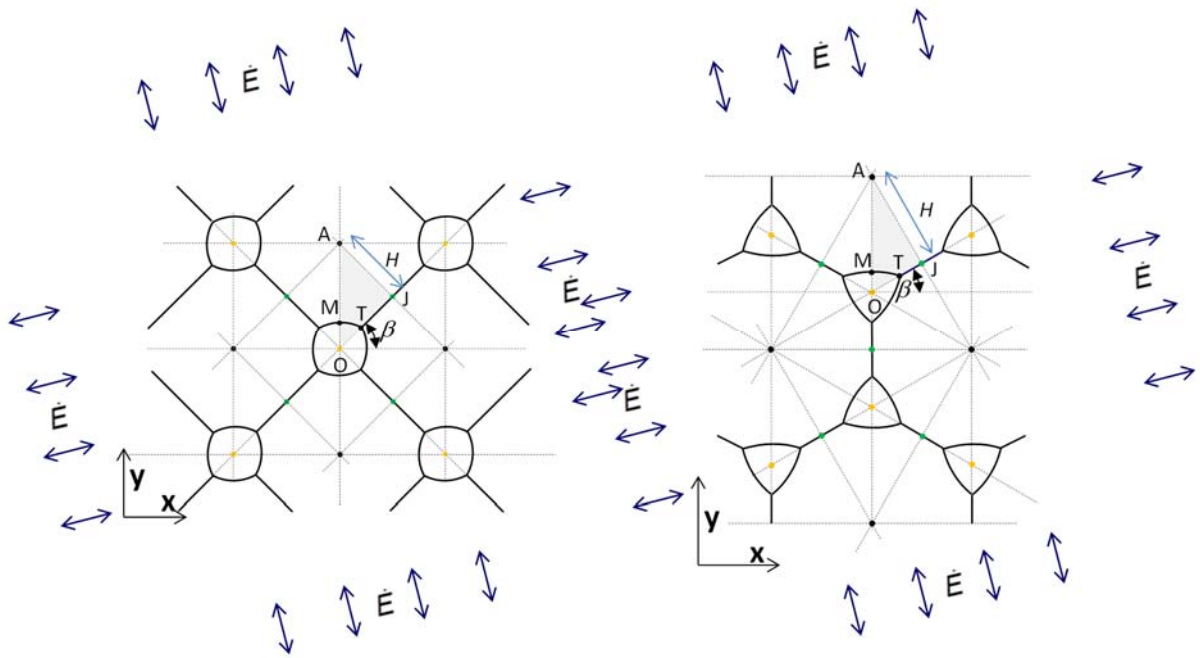


Figure 2: Arrays of identical grains with $Z = 4$ and 6 under radial strain rate \dot{E} . RVEs are triangles in grey shade.

During densification or expansion of the aggregate, the average grain coordination varies monotonously as a function of relative density. Still, a system with arbitrary, non-integer

average coordination can be modelled in 2D by considering a triangular RVE with H and β defined via Eqs. (1) and (2) with non-integer Z . Fig. 3a represents, such an RVE in the case of convex pore curvature with $\dot{E} < 0$, i.e. during densification. The curve drawn in red is the actual pore profile during densification whereas the dashed curve in black is the static equilibrium profile at the same relative density ρ . The latter is an arc of circle of radius denoted R_e . $\kappa_e = \frac{1}{R_e}$ is the curvature of the static profile whereas κ_T denotes the curvature of the profile at triple line T. T_e and M_e are the positions of points T and M at static equilibrium. The azimuthal angle spanning the static profile from M_e to T_e is

$$\varphi_{Te} = \frac{\psi}{2} - \beta \quad (5)$$

Hence, $\varphi_{Te} > 0$ in case of a convex pore and $\varphi_{Te} < 0$ in case of concave pore. Axis \mathbf{y} is taken parallel to OA. With respect to O, the position of the centre of curvature of the equilibrium profile is the vector

$$\mathbf{P}_e = -R_e \frac{\cos(\varphi_{Te} + \beta)}{\cos \beta} \mathbf{y} = -R_e \frac{\cos \frac{\psi}{2}}{\cos \beta} \mathbf{y} \quad (6)$$

R_e is related to ρ , Z , H and ψ via

$$\begin{aligned} 1 - \rho &= \frac{1}{H^2 \tan \beta} \left(\int_0^{\varphi_{Te}} R_e^2(\varphi) d\varphi - R_e^2 \frac{\cos(\varphi_{Te} + \beta)}{\cos \beta} \sin \varphi_{Te} \right) \\ &= \frac{R_e^2}{H^2} \xi_e \end{aligned} \quad (7)$$

$$\text{with} \quad \xi_e = \frac{1}{\tan \beta} \left(\varphi_{Te} - \frac{\cos(\varphi_{Te} + \beta) \sin \varphi_{Te}}{\cos \beta} \right) \quad (8)$$

We denote B the distance from point J along grain boundary: $B = 0$ at J and $B = B_T$ at T. B_T thus denotes half of the grain boundary length. At static equilibrium, $B_T = B_{Te}$ with

$$B_{Te} = H \tan \beta - R_e \frac{\sin \varphi_{Te}}{\cos \beta} \quad (9)$$

In the case represented in Fig. 3a, $B_T > B_{Te}$ and $\kappa_T < \kappa_e = \frac{1}{R_e}$ because, as $\dot{E} < 0$, matter diffuses along pore surface from T to M, which implies an increase of κ from T to M. The reverse applies if $\dot{E} > 0$. Eqs. (6) to (9) are valid for convex pores as well as for concave pores if one takes $R_e > 0$ for a convex pore and $R_e < 0$ for a concave pore. ξ_e is always positive owing to the change of sign of φ_{Te} when the sign of curvature changes. In this paper, these conventions for the sign of curvature and for the sign of φ are followed everywhere in such a way that all equations be valid in the whole range of dihedral angles $0 \leq \psi \leq 2\pi$.

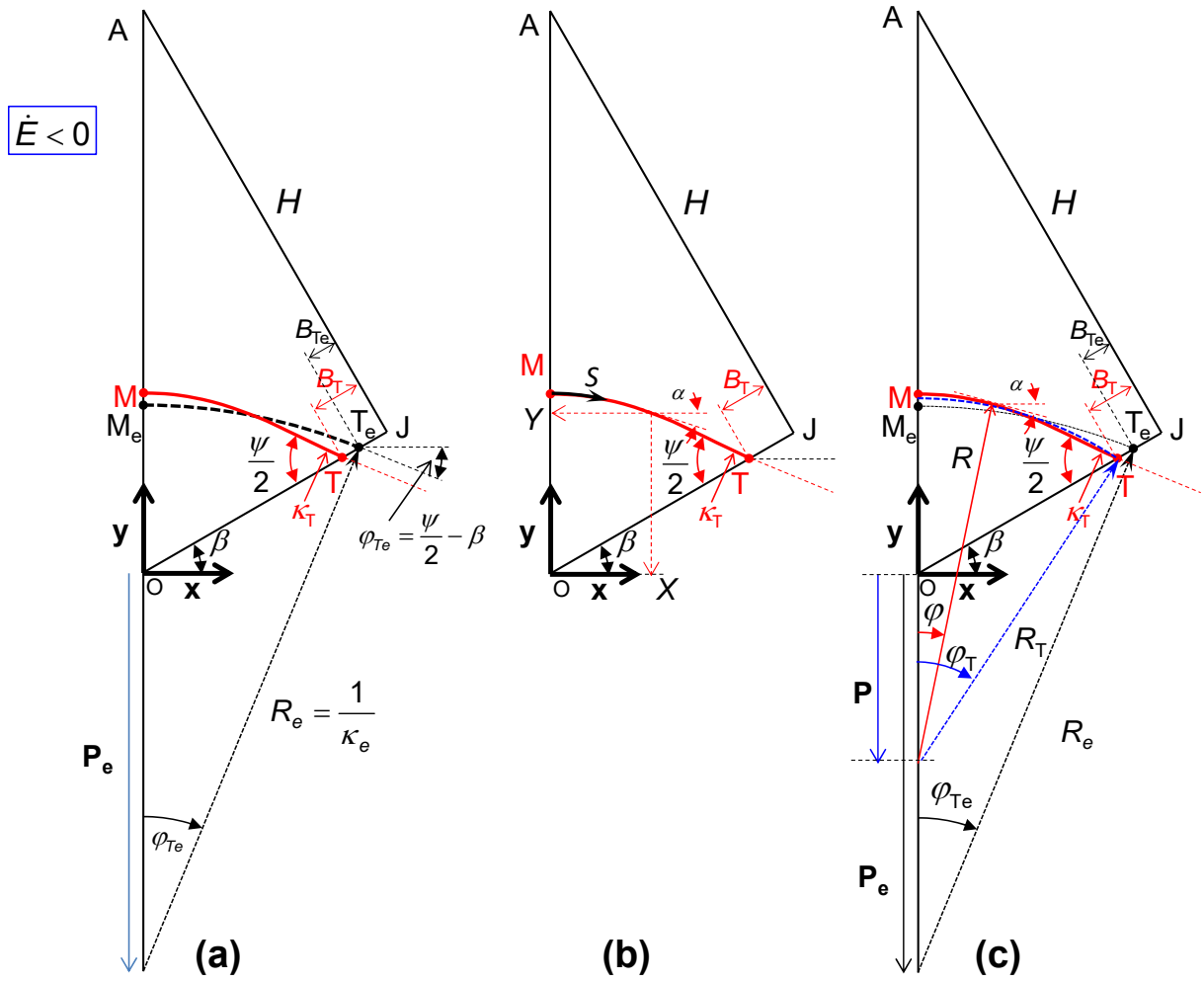


Figure 3 : RVE in the case of convex pore curvature with $\dot{E} < 0$. (a) Dynamic and static profile parameters. (b) Cartesian coordinates X and Y and current coordinate S . (c) Polar coordinates R and ϕ .

2.2. Resolution in Cartesian coordinates

2.2.1. Partial differential equation

The following mathematics is written for the case of a convex pore such as represented in Fig.

3b. The Cartesian coordinates of the points on pore profile are denoted X and Y whereas the coordinate along the profile is denoted S , which spans the range $S_{X=0} = 0 \leq S \leq S_{X=X_T} = S_T$.

With respect to the centre of the coordinate system (point O), the velocity $\dot{\mathbf{u}}(S, t)$ of the points

on the pore surface is the sum of two vectors

$$\begin{aligned}\dot{\mathbf{u}}(\mathbf{S},t) &= \dot{X}(\mathbf{S},t)\mathbf{x} + \dot{Y}(\mathbf{S},t)\mathbf{y} \\ &= \dot{\mathbf{u}}_{tr}(t) + \dot{\mathbf{u}}_{diff}(\mathbf{S},t)\end{aligned}\quad (10)$$

$\dot{\mathbf{u}}_{tr}(t)$ is the velocity of translation of the profile due to the divergence of the diffusion flux j_{gb} along grain boundaries. It is oriented along axis \mathbf{y} and writes

$$\dot{\mathbf{u}}_{tr}(t) = \frac{\dot{H}(t)}{\cos\beta}\mathbf{y} = \dot{E}(t)\frac{H(t)}{\cos\beta}\mathbf{y} \quad (11)$$

$\dot{\mathbf{u}}_{diff}(\mathbf{S},t)$ is the apparent velocity of displacement of the surface due to the divergence of the diffusion flux j_s . Denoting \mathbf{n} the outward normal to the pore surface, it can be expressed as

$\dot{\mathbf{u}}_{diff}(\mathbf{S},t) = \dot{u}_{diff}(\mathbf{S},t)\mathbf{n}$, with (e.g. [32]):

$$\dot{u}_{diff}(\mathbf{S},t) = \Omega \frac{\partial j_s}{\partial S}(\mathbf{S},t) \quad (12)$$

where Ω is the volume of the diffusing species. By convention, we have taken the diffusion flux j_s to be positive when oriented away from the triple line, i.e. when oriented from T to M (the same convention will apply for the flux j_{gb}). The surface diffusion flux is related to the curvature gradient by the linear kinetic model:

$$j_s(\mathbf{S},t) = -\frac{1}{\Delta} \frac{\delta D_{gb} \gamma_s}{kT} \frac{\partial \kappa}{\partial S}(\mathbf{S},t) \quad (13)$$

where $\kappa(\mathbf{S},t)$ is the curvature of the pore surface. The normal to the pore surface expresses as:

$$\mathbf{n}(\mathbf{S},t) = -\sin\alpha(\mathbf{S},t)\mathbf{x} - \cos\alpha(\mathbf{S},t)\mathbf{y} \quad (14)$$

$$\text{with} \quad \alpha(\mathbf{S},t) = \arctan\left(-\frac{\partial Y}{\partial X}\right). \quad (15)$$

Combining the previous relations, we can write:

$$\dot{\mathbf{u}}_{diff}(S,t) = -\left(-\sin\alpha(S,t)\mathbf{x} - \cos\alpha(S,t)\mathbf{y}\right) \frac{1}{\Delta} \frac{\delta D_{gb}\gamma_s\Omega}{kT} \frac{\partial^2 \kappa(S,t)}{\partial S^2} \quad (16)$$

By projecting of $\dot{\mathbf{u}}(S,t)$ on the directions normal and tangent to the profile, one obtains the set of two equations (omitting mention of variables t and S)

$$\dot{X} \sin\alpha + \left(\dot{Y} - \frac{\dot{H}}{\cos\beta}\right) \cos\alpha = -\dot{u}_{diff} \quad (17)$$

$$\text{and} \quad \dot{X} \cos\alpha - \left(\dot{Y} - \frac{\dot{H}}{\cos\beta}\right) \sin\alpha = 0 \quad (18)$$

$$\text{Hence,} \quad \dot{X} = \left(\dot{Y} - \frac{\dot{H}}{\cos\beta}\right) \tan\alpha \quad (19)$$

and Eqs (16) and (17) yield the PDE of pore profile as

$$\dot{Y}(S,t) - \frac{\dot{H}(t)}{\cos\beta} - \frac{1}{\Delta} \frac{\delta D_{gb}\gamma_s\Omega}{kT} \cos\alpha(S,t) \frac{\partial^2}{\partial S^2} \kappa(S,t) = 0 \quad (20)$$

$\kappa(S,t)$ can be developed into a function of $\frac{\partial Y(S,t)}{\partial S}$ and $\frac{\partial^2 Y(S,t)}{\partial S^2}$. Eq. (20) is thus a non-

linear PDE of the fourth order with respect to S . The solution of this PDE is submitted to an initial condition for the shape of the profile:

$$Y(S,t=0) = Y_0(S) \quad (21)$$

and to four boundary conditions:

$$[1] \alpha_{S=0} = 0, \quad (22)$$

$$[2] \alpha_{S=S_T} = \frac{\psi}{2} - \beta, \quad (23)$$

$$[3] j_{sS=0} = -\frac{1}{\Delta} \frac{\delta D_{gb}\gamma_s}{kT} \left(\frac{\partial \kappa}{\partial S}\right)_{S=0} = 0 \quad (24)$$

$$[4] j_{sS=S_T} = -\frac{1}{2} j_{gbT} = -\frac{1}{\Delta} \frac{\delta D_{gb} \gamma_s}{kT} \left(\frac{\partial \kappa}{\partial S} \right)_{S=S_T} = -\frac{1}{\Omega} B_T \dot{H} \quad (25)$$

(for the continuity at T of the surface and grain boundary diffusion fluxes j_s and j_{gb})

As $\dot{H} = 0$ when $\dot{E} = 0$, it is easy to see that, if $\dot{E} = 0$, the solutions of Eq. (20) tend asymptotically to a static arc of circle.

2.2.2. Numerical analysis of the pore profile evolution

Using Eq. (20), the evolution of the pore profile can be calculated numerically using a finite difference method similar to the method used by Svoboda and Riedel [29]. Consider a spatial discretization of the profile in $(N+1)$ nodes. At every simulation time step Δt , the new coordinates (X_i, Y_i) of node i ($i=0, \dots, N-1$) are updated using an full-explicit Euler scheme:

$$\begin{aligned} X_i^{(n+1)} &= X_i^{(n)} + \dot{u}_{diff,i} n_{x,i} \Delta t \\ Y_i^{(n+1)} &= Y_i^{(n)} + \dot{u}_{diff,i} n_{y,i} \Delta t + \frac{\dot{E}H}{\cos \beta} \Delta t \end{aligned} \quad (26)$$

where the subscript n refers to the time step and the subscript i to the node index. The diffusion velocity is given by

$$\dot{u}_{diff} = -\frac{1}{\Delta} \frac{\Omega \delta D_{gb} \gamma_s}{kT} \frac{d^2 \kappa}{dS^2} \quad (27)$$

The curvature second derivative relative to the arc length is approximate as follows. First the curvature at a node $i=0, \dots, N$ is estimated from the curvature of the parabola passing through the points $(i-1, i, i+1)$ (for the node $i=0$, the symmetry condition is used). The normal components at the nodes are also calculated. Next, the curvature $\kappa(S)$ near an interior node i is interpolated by another parabola passing through the points $\kappa(S_{i-1})$, $\kappa(S_i)$ and $\kappa(S_{i+1})$ to calculate the second derivative.

A special treatment is applied to adjust the position of the triple point $i = N$ at each time step in order to satisfy the condition of conservation of mass Eq. (25). For a given value of the coordinate X_T , we must have $Y_T = X_T \tan(\beta)$. The curvature at the triple point is then approximated by the curvature of a parabola passing through nodes $N - 1$ and N , and with slope given by Eq. (23) at the triple point. Finally, the surface flux at the triple point is calculated from the constitutive equation. The position X_T is adjusted iteratively (using Newton's method) until condition (25) is satisfied.

About 50 nodes were used in the simulations, which was found sufficient to ensure convergence of the results. The method is subjected to the usual restriction on the time step to keep the integration stable [33]. We also found necessary to remesh the pore profile at regular intervals in order to maintain a more or less constant and uniform mesh size.

2.3. Resolution in polar coordinates

2.3.1. Partial differential equation

It is helpful to express the problem in an alternative way using a system of polar coordinates that most closely fits the evolution pore profile during deformation. For this purpose, we locate the pole of the coordinates on the \mathbf{y} axis at point P such that an arc of circle of radius R_T centred in P and passing by point T circumscribes the same pore volume as the actual profile (Fig. 3c). The azimuthal angle then spans the range $\varphi_{X=0} = 0 \leq \varphi \leq \varphi_{X=X_T} = \varphi_T$. Eqs. (6) to (9) translate into

$$\mathbf{P}(t) = -R_T(t) \frac{\cos(\varphi_T(t) + \beta)}{\cos \beta} \mathbf{y} \quad (28)$$

$$1 - \rho(t) = \frac{R_T(t)^2}{H(t)^2} \xi_T(t) \quad (29)$$

$$\text{with } \xi_T(t) = \frac{1}{\tan \beta} \left(\varphi_T(t) - \frac{\cos(\varphi_T(t) + \beta) \sin \varphi_T(t)}{\cos \beta} \right) \quad (30)$$

$$\text{and } B_T(t) = H(t) \tan \beta - R_T(t) \frac{\sin \varphi_T(t)}{\cos \beta} \quad (31)$$

$R_T(t)$ tends to $R_e(t)$ and $\varphi_T(t)$ tends to φ_{Te} when \dot{E} tends to zero. If $\dot{E} < 0$, $R_T(t) < R_e(t)$, hence, from Eqs. (7) and (29), $\varphi_T(t) < \varphi_{Te}$ (Fig. 3c), and reversely if $\dot{E} > 0$. This applies also for concave pores if one accounts for the change of the sign of R_T , R_e , φ_T and φ_{Te} .

The coordinates X and Y of the points on the profile then write

$$X(S, t) = R(S, t) \sin \varphi \quad (32)$$

$$Y(S, t) = R(S, t) \cos \varphi - R_T(t) \frac{\cos(\varphi_T(t) + \beta)}{\cos \beta} \quad (33)$$

For simplifying the expression of partial derivatives with respect to S and φ , we make use of the

notations: $\frac{\partial R}{\partial \varphi} \equiv R_\varphi$, $\frac{\partial^2 R}{\partial \varphi^2} \equiv R_{\varphi\varphi}$, $\frac{\partial Y}{\partial S} \equiv Y_S$, $\frac{\partial \varphi}{\partial S} \equiv \varphi_S$, etc.. The profile slope (Eq. (15)) then

becomes (omitting mention of variables t and S)

$$\begin{aligned} \alpha &= \arctan \left(-\frac{Y_\varphi}{X_\varphi} \right) \\ &= \arctan \left(-\frac{R_\varphi \cos \varphi - R \sin \varphi}{R_\varphi \sin \varphi + R \cos \varphi} \right) \\ &= \varphi - \zeta \end{aligned} \quad (34)$$

$$\text{with } \zeta = \arctan \left(\frac{R_\varphi}{R} \right) \quad (35)$$

i.e.
$$\cos \zeta = \frac{1}{\sqrt{1 + \left(\frac{R_\varphi}{R}\right)^2}} = R\varphi_S \quad (36)$$

The boundary conditions are

at $\varphi = 0$, $\alpha_M = 0$, hence $\zeta_M = 0$ (37)

at $\varphi = \varphi_T$, $\alpha_T = \varphi_{Te} = \frac{\psi}{2} - \beta$, hence $\zeta_T = \varphi_T - \varphi_{Te}$ (38)

Denoting $\dot{R}_T \equiv \frac{dR_T}{dt}$ and $\dot{\varphi}_T \equiv \frac{d\varphi_T}{dt}$, the components of the velocity of displacement of the profile write, from Eqs. (32) and (33),

$$\dot{X} = \dot{R} \sin \varphi + R \dot{\varphi} \cos \varphi \quad (39)$$

and
$$\dot{Y} = \dot{R} \cos \varphi - R \dot{\varphi} \sin \varphi - \frac{1}{\cos \beta} \left(\cos(\varphi_T + \beta) \dot{R}_T - R_T \sin(\varphi_T + \beta) \dot{\varphi}_T \right) \quad (40)$$

which, for concision, will be written

$$\dot{Y} = \dot{R} \cos \varphi - R \dot{\varphi} \sin \varphi - \dot{R}_T \frac{a}{\cos \beta} \quad (41)$$

with
$$a = \cos(\varphi_T + \beta) - \frac{R_T}{\dot{R}_T} \dot{\varphi}_T \sin(\varphi_T + \beta) \quad (42)$$

Via Eqs. (39) and (41), Eqs (17) and (18) translate into

$$\dot{R} \cos \zeta - R \dot{\varphi} \sin \zeta - \frac{\cos(\varphi - \zeta)}{\cos \beta} (a \dot{R}_T + \dot{H}) = -\dot{u}_{diff} \quad (43)$$

and
$$\dot{R} \sin \zeta + R \dot{\varphi} \cos \zeta + \frac{1}{\cos \beta} (a \dot{R}_T + \dot{H}) \sin \alpha = 0 \quad (44)$$

Finally, combining Eqs. (43) and (44) and making use of Eq. (19) yield the PDE of the profile in the form

$$\dot{R}(\varphi, t) - \frac{\dot{R}_T(t)}{\cos \beta} \left(a(t) + \frac{\dot{H}(t)}{\dot{R}_T(t)} \right) \cos \varphi - \frac{1}{\Delta} \frac{\delta D_{gb} \gamma_s \Omega}{kT} \cos \zeta(\varphi, t) \frac{\partial^2 \kappa(\varphi, t)}{\partial S^2} = 0 \quad (45)$$

Eq. (45) can be developed into a PDE of the sole function $R(\varphi, t)$ via the expression of $\kappa(\varphi, t)$ in polar coordinates:

$$\kappa = \frac{1}{R} \frac{1 + 2 \left(\frac{R_\varphi}{R} \right)^2 - \frac{R_{\varphi\varphi}}{R}}{\left(1 + \left(\frac{R_\varphi}{R} \right)^2 \right)^{\frac{3}{2}}} \quad (46)$$

and via the relationship

$$\begin{aligned} \frac{\partial^2 \kappa}{\partial S^2} &= \frac{\partial}{\partial S} \left(\frac{\partial \kappa}{\partial \varphi} \varphi_s \right) \\ &= \varphi_s \frac{\partial}{\partial S} \left(\frac{\partial \kappa}{\partial \varphi} \right) + \frac{\partial \kappa}{\partial \varphi} \varphi_{ss} \\ &= \varphi_s^2 \frac{\partial^2 \kappa}{\partial \varphi^2} + \varphi_s \frac{d\varphi_s}{d\varphi} \frac{\partial \kappa}{\partial \varphi} \end{aligned} \quad (47)$$

Eq. (45) is thus a non-linear PDE of the fourth order with respect to the variable φ . The solution is submitted to a condition for the shape of the profile at the initial relative density ρ_{in} . If, for example, the initial profile was at static equilibrium with uniform radius of curvature $(R_e)_{\rho_{in}}$ (Eq. (7)), the initial condition would write

$$R(\varphi, t=0) = (R_e)_{\rho_{in}} \quad (48)$$

The PDE is also submitted to the following four boundary conditions:

$$[1] \alpha_{\varphi=0} = 0, \text{ i.e. } \zeta_{\varphi=0} = 0 \text{ (confer Eq. (34))} \quad (49)$$

$$[2] \alpha_{\varphi=\varphi_T} = \frac{\psi}{2} - \beta, \text{ i.e. } \zeta_{\varphi=\varphi_T} = \varphi_T - \frac{\psi}{2} - \beta \quad (50)$$

$$[3] j_{s\varphi=0} = -\frac{1}{\Delta} \frac{\delta D_{gb} \gamma_s}{kT} \left(\frac{\partial \kappa}{\partial S} \right)_{\varphi=0} = 0 \quad (51)$$

$$[4] j_{s\varphi=\varphi_T} = -\frac{1}{2} j_{gbT} = -\frac{1}{\Delta} \frac{\delta D_{gb} \gamma_s}{kT} \left(\frac{\partial \kappa}{\partial S} \right)_{\varphi=\varphi_T} = -\frac{1}{\Omega} G_T \dot{H} \quad (52)$$

2.3.2. Asymptotic solution

Whatever the initial shape of the pore profile, if diffusivity ratio Δ tends to zero, the profile tends asymptotically (in time) to the arc of circle $R(\varphi, t) = R_e(t) = R_T(t)$. The asymptotic form of Eq. (45) would then tend to

$$\dot{R}_e(t) - \frac{\dot{R}_e(t)}{\cos \beta} \left(\cos \frac{\psi}{2} + \frac{\dot{H}(t)}{\dot{R}_e(t)} \right) \cos \varphi - \frac{1}{\Delta} \frac{\delta D_{gb} \gamma_s \Omega}{kT} \cos \zeta \frac{\partial^2 \kappa(\varphi, t)}{\partial S^2} = 0 \quad (53)$$

(the third term would be indefinite). The fact that $[\dot{R}(\varphi, t)]_{\text{asymptotic}}$ tends to $\dot{R}_e(t)$ when Δ tends to zero indicates that the dependence of $[\dot{R}(\varphi, t)]_{\text{asymptotic}}$ on φ is weak as long as Δ is small. This prompts us to calculate the asymptotic solution of Eq. (45) for small Δ values by making use of the approximation $\dot{R}(\varphi, t) \cong \dot{R}_\infty(t)$ where $R_\infty(t)$ is a function that complies with boundary conditions and tends to $R_e(t)$ when Δ tends to zero. In Section 3.1, the validity of this approximation will be assessed by comparison with numerical calculations using the finite difference method. The asymptotic form of Eq. (45) then writes

$$\dot{R}_\infty(t) - \frac{\dot{R}_T(t)}{\cos \beta} \left(a(t) + \frac{\dot{H}(t)}{\dot{R}_T(t)} \right) \cos \varphi - \frac{1}{\Delta} \frac{\delta D_{gb} \gamma_s \Omega}{kT} \cos \zeta(\varphi, t) \frac{\partial^2 \kappa(\varphi, t)}{\partial S^2} = 0. \quad (54)$$

$\dot{R}_e(t)$ and $\dot{H}(t)$ are linked to \dot{E} via Eqs (2), (3), (4), and (7)). \dot{E} being an imposed parameter, Eq. (54) is an ordinary differential equation (ODE) of the fourth order with respect to S . This ODE is submitted to the same boundary conditions as the general PDE (Eqs. (49) to (52)), but not to the initial condition. Hence, the rate of evolution of the asymptotic profile results only

from the dependence on \dot{E} of both the source term $\frac{\dot{R}_T(t)}{\cos\beta} \left(a(t) + \frac{\dot{H}(t)}{\dot{R}_T(t)} \right) \cos\varphi$ and the

boundary condition Eq. (51). As

$$\frac{\partial^2 R(\varphi, t)}{\partial S \partial t} = \frac{\partial}{\partial t} \left(\frac{\partial R(\varphi, t)}{\partial S} \right) = \frac{\partial \sin(-\alpha(\varphi, t))}{\partial t} \cong -\frac{\partial \alpha(\varphi, t)}{\partial t}, \quad (55)$$

the approximation $\dot{R}(\varphi, t) \cong \dot{R}_\infty(t)$ amounts to the approximation $\alpha(\varphi, t) \cong \alpha_\infty(\varphi)$. Hence, as long as Δ is not too large, asymptotic profiles for different relative densities are close to be self-similar (like the arcs of circle of static profiles).

With some additional approximation, Eq. (54) can be resolved analytically. The mathematical development underlying this resolution is presented in Appendices 1 and 2. Appendix 1

develops the factor $\left(a + \frac{\dot{H}}{\dot{R}_T} \right)$ in the source term by further relying on the approximation

$\dot{R}(\varphi, t) \cong \dot{R}_\infty(t)$. Appendix 2 presents the analytical procedure of resolution of Eq. (54). The additional approximation to be introduced for this purpose is

$$1 + \left(\frac{R_\varphi}{R} \right)^2 = 1 + (\tan \zeta)^2 \cong 1, \quad (56)$$

which also means as a corollary

$$\cos \zeta = \frac{R d\varphi}{dS} \cong 1. \quad (57)$$

These approximations hold as long as the departure of the profile from an arc of circle is small enough, i.e. as long as the product $\|\dot{E}\Delta\|$ is small enough. It is found that it follows from boundary conditions that $\dot{R}_\infty = \dot{R}_T$ (Eqs. (A2.3) and (A2.8)). For given values of ρ , Z , \dot{E} and Δ , the resolution procedure leads to closed form expressions for the diffusion flux $j_s(\varphi)$ (Eq.

(A2.6)), the surface curvature $\kappa(\varphi)$ (Eq. (A2.10)), the profile slope $\alpha(\varphi)$ (Eq. (A2.13)), the radial coordinate $R(\varphi)$ (Eq. (A2.16)), and the difference $\varphi_{Te} - \varphi_T$ (Eq. (A2.20)). The parameters φ_T , H , R_T , ξ_T , a , ξ^* , and c involved in the equations are calculated as follows:

For given ρ , Z , \dot{E} and Δ ,

(1) calculate φ_T by numerical resolution of Eq. (A2.20)

(2) calculate H via Eqs. (1) and (2)

(3) calculate (i) R_T via Eq. (29)

(ii) ξ_T via Eq. (30)

(iii) a via Eq. (42)

(iv) ξ^* via Eq. (A1.10)

(v) c via Eq. (A2.4)

Asymptotic profiles presented in Section 3 are drawn using Eq. (A2.16) for $R(\varphi)$ together with Eq. (28) for the position of the pole. In Ref [31], computation of bulk viscosity will also make use of Eq. (31) for the grain boundary size, B_T , and Eq. (A2.14) for the pore curvature at triple line, κ_T .

2.3.3. Damping rate of the transient component of the general solution

The transient component of the solution of Eq. (45) is the difference between the general solution and the asymptotic solution. As Eq. (45) can be resolved only via full numerical computation, the transient component should be derived numerically. Nevertheless, if $\dot{E} = 0$, Eq. (45) reduces to the homogeneous PDE

$$\dot{R}(\varphi, t) - \frac{1}{\Delta} \frac{\delta D_{gb} \gamma_s \Omega}{kT} \cos \zeta(\varphi, t) \frac{\partial^2 \kappa(\varphi, t)}{\partial S^2} = 0 \quad (58)$$

As shown below, this PDE can be resolved exactly using classical methods of variable separation. We will assume that, at given ρ , the damping rate of the solution of Eq. (45) for $\dot{E} \neq 0$ is well approximated by the damping rate of the solution of Eq. (58) at the same relative density ρ .

Taking the partial derivative of the two members with respect to S and accounting for Eq. (54) as well as for the relation

$$\kappa = \frac{\partial \alpha}{\partial S}, \quad (59)$$

Eq. (58) becomes

$$\dot{\alpha}(\varphi, t) + \frac{1}{\Delta} \frac{\delta D_{gb} \gamma_s \Omega}{kT} \cos \zeta(\varphi, t) \frac{\partial^4 \alpha(\varphi, t)}{\partial S^4} = 0 \quad (60)$$

The solution of this PDE is submitted to the initial condition

$$\alpha(\varphi, t = 0) = \alpha_0(\varphi) \quad (61)$$

and, according to Eqs (49) to (52), to the boundary conditions

$$\alpha_{\varphi=0} = 0, \quad \alpha_{\varphi=\varphi_T} = \frac{\psi}{2} - \beta, \quad \left(\frac{\partial^2 \alpha}{\partial S^2} \right)_{\varphi=0} = 0, \quad \left(\frac{\partial^2 \alpha}{\partial S^2} \right)_{\varphi=\varphi_T} = 0 \quad (62)$$

The asymptotic solution of Eq. (60) is $\alpha(\varphi) = \varphi$. Boundary conditions (61) express the fact that the transient behaviour amounts to a simple redistribution of matter on the pore surface, without diffusion flux along grain boundary. As noticed in the introduction, this transient behaviour is considered to dominate during the initial stage of sintering whereas the strain-rate-controlled behaviour represented by the asymptotic solution dominates during the intermediate stage (pore closure transition does not exist in 2D).

It is convenient to transform the variable S into $s = \frac{S}{S_T}$ in such a way as to keep, whatever the

value of ρ , the same boundaries $0 \leq s \leq 1$ for the domain of the solution. In addition, we

define a non-dimensional time $\tau = \frac{t}{t^s}$ where

$$t^s = \Delta \frac{kTS_T^4}{\Omega \delta D_{gb} \gamma_s} \quad (63)$$

is a characteristic time for surface diffusion. If one adopts approximation (57), Eq. (60) then writes

$$\frac{\partial \alpha}{\partial \tau} = -\frac{\partial^4 \alpha}{\partial s^4} \quad (64)$$

The homogeneous PDE Eq. (64) lends itself to the classical method of separation of the variables and of expression of the solution as a series expansion of eigenvalues. The solution complying with initial and boundary conditions (Eqs (61) and (62)) writes

$$\alpha(\varphi) - \varphi = \sum_{n=1}^{\infty} I_n e^{-\lambda_n^4 \tau} \sin(\lambda_n s) \quad (65)$$

$$\text{with} \quad \lambda_n = n\pi \quad (66)$$

$$\text{and} \quad I_n = \frac{1}{S_T} \int_0^{S_T} [\alpha_0(\varphi) - \varphi] \sin(\lambda_n s) dS \quad (67)$$

The rate of damping of Eq. (64) is dominated by the rate of damping of term $n = 1$ in the series expansion. It can thus be estimated as

$$\frac{1}{\alpha(\varphi) - \varphi} \frac{\partial [\alpha(\varphi) - \varphi]}{\partial t} \cong -\frac{\pi^4}{t^s} \quad (68)$$

The profile being not an arc of circle, we write

$$S_T = f R_T \varphi_T \quad (69)$$

where f is a correction factor larger than 1, which decreases during the evolution towards the asymptotic regime. Via Eqs. (2), (29), and (30), Eq. (68) then translates into

$$\frac{1}{\alpha(\varphi) - \varphi} \frac{\partial [\alpha(\varphi) - \varphi]}{\partial t} \cong - \frac{\pi^2}{\Delta} \frac{Z^2}{(f\varphi_T)^4} \left(\varphi_T - \frac{\cos(\varphi_T + \beta) \sin \varphi_T}{\cos \beta} \right)^2 \left(\frac{\rho}{1 - \rho} \right)^2 \frac{1}{t^{gb}} \quad (70)$$

in which we have used the definition of the characteristic time for grain boundary diffusion

$$t^{gb} = \frac{kTR_G^4}{\Omega \delta D_{gb} \gamma_s} \quad (71)$$

(the superscript t^{gb} is used in order to avoid confusion with the characteristic time t^s defined in Eq. (63)). The accuracy of Eq. (70) as an estimate of the damping rate of the transient component of the general solution of Eq. (45) with $\dot{E} \neq 0$ will be assessed in Section 3.1.

3. Results and discussion

3.1. Evolution of pore profile during sintering

Figs. 4 to 7 present the evolution of pore profiles during densification at a rate

$\dot{E} = -1350 \left(t^{gb} \right)^{-1}$ with $\Delta = 0.1$ and $Z = 6$. The exact profiles (full curves) calculated via the

finite difference method according to Section 2.2.2 are compared to the asymptotic profiles

(dashed curves) calculated according to Section 2.3.2. R_G is the unit of length. In the four

cases, initial density is $\rho = 0.907$. Dihedral angle is $\psi = 180^\circ$ in Figs 4 and 5, $\psi = 105^\circ$ in Fig. 6,

and $\psi = 30^\circ$ in Fig. 7. In Figs. 4, 6, and 7, the initial profile is largely out of equilibrium: it is

drawn to correspond to cylinders (i.e. convex arcs of circle) which are in contact via very small grain boundaries surrounded by a concave neck complying with dihedral angle along triple line.

In Fig. 5, the initial profile is taken to be the (concave) arc of circle corresponding to static

equilibrium. Asymptotic profiles are thus identical in Figs 4 and 5. Conspicuously, whatever the initial profile and the dihedral angle, exact profiles calculated numerically quickly converge toward asymptotic profiles when densification progresses. This observation gives strong support to the validity of the approximations underneath both the definition of the asymptotic ODE Eq. (54) and the procedure for the semi-analytical resolution of this ODE.

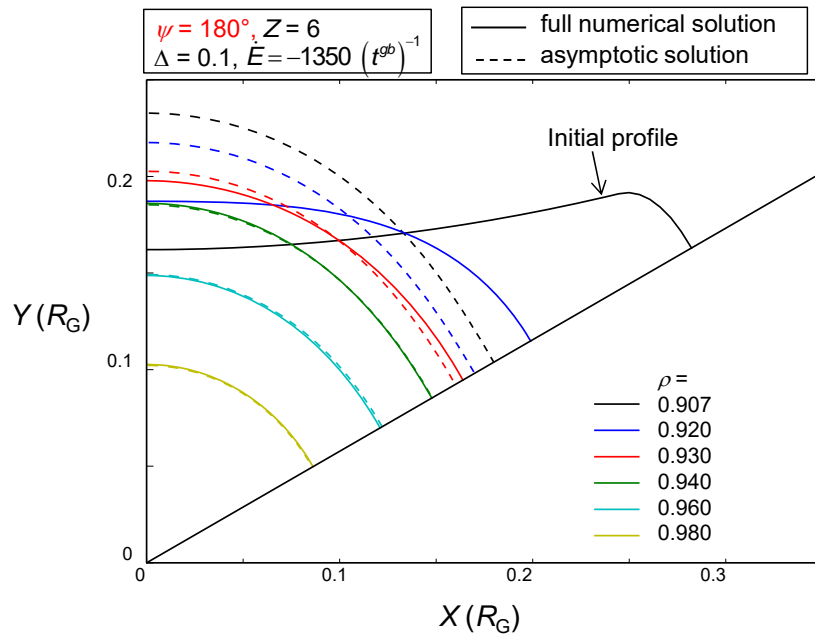


Figure 4: Evolution of pore profiles for $\psi = 180^\circ$ during densification at $\dot{E} = -1350 (t^{gb})^{-1}$ with $\Delta = 0.1$ and $Z = 6$. Initial density is $\rho = 0.907$. The initial profile presents a small neck close to particle contact. Asymptotic profiles (dashed curves) calculated according to Eq. (A2.16) are compared to the exact profiles (full curves) calculated via the finite difference method.

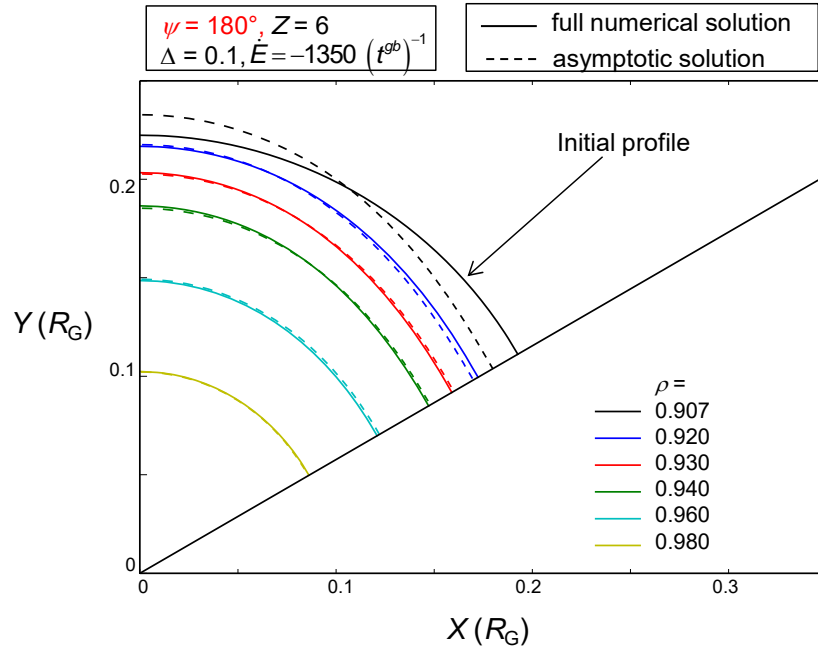


Figure 5: Evolution of pore profiles for $\psi = 180^\circ$ during densification at $\dot{E} = -1350 (t^{gb})^{-1}$ with

$\Delta = 0.1$ and $Z = 6$. Initial density is $\rho = 0.907$. The initial profile is the arc of circle of static equilibrium. Asymptotic profiles (dashed curves) calculated according to Eq. (A2.16) are compared to the exact profiles (full curves) calculated via the finite difference method.

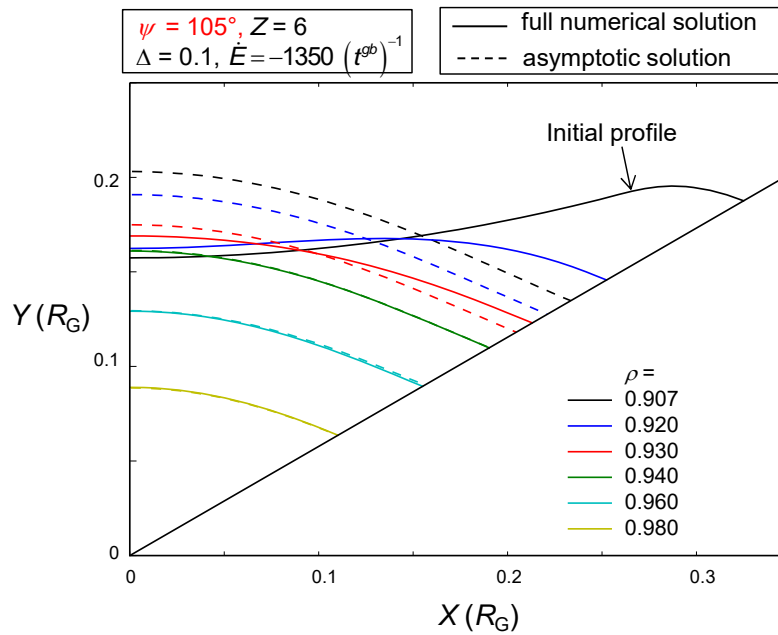


Figure 6: Evolution of pore profiles for $\psi = 105^\circ$ during densification at $\dot{E} = -1350 (t^{gb})^{-1}$ with

$\Delta = 0.1$ and $Z = 6$. Initial density is $\rho = 0.907$. The initial profile presents a small neck close to particle contact. Asymptotic profiles (dashed curves) calculated according to Eq. (A2.16) are compared to the exact profiles (full curves) calculated via the finite difference method.

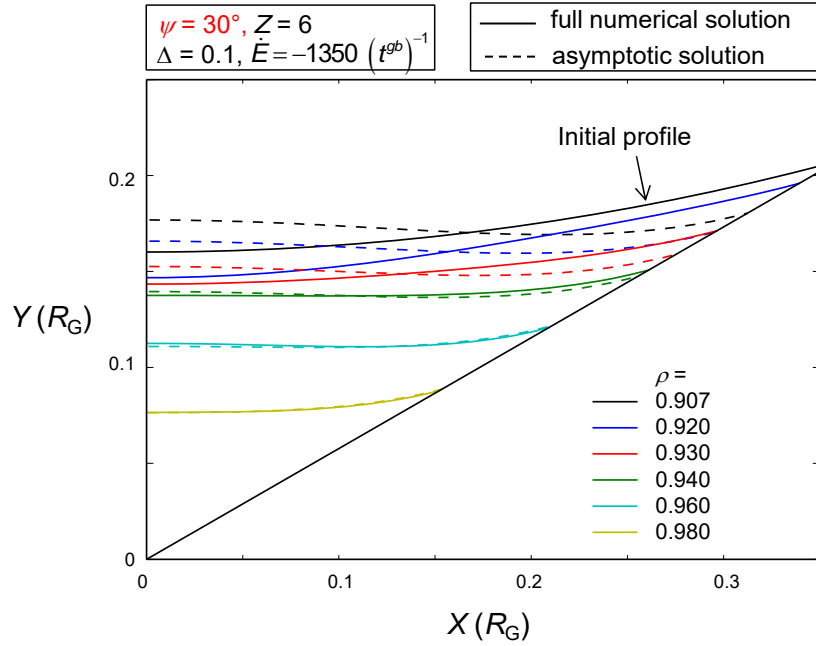


Figure 7: Evolution of pore profiles for $\psi = 30^\circ$ during densification at $\dot{E} = -1350(t^{gb})^{-1}$ with $\Delta = 0.1$ and $Z = 6$. Initial density is $\rho = 0.907$. The initial profile presents a small neck close to particle contact. Asymptotic profiles (dashed curves) calculated according to Eq. (A2.16) are compared to the exact profiles (full curves) calculated via the finite difference method.

Fig. 8 presents a comparison of exact profiles (full curves) and asymptotic profiles (dashed curves) during expansion at a rate $\dot{E} = 900(t^{gb})^{-1}$ with $\Delta = 0.1$, $Z = 6$, and $\psi = 180^\circ$. Initial density is $\rho = 0.980$. The initial profile is the arc of circle corresponding to static equilibrium (it would not make sense to consider a non-equilibrium initial profile at high density). The asymptotic profile does not much differ from the initial profile at $\rho = 0.980$ and, when the system expands, the departure between exact profiles and asymptotic profiles remains very

small (notice that, at low ρ , both profiles strongly differ from arcs of circle). The results under expansion for $\psi = 180^\circ$ and $\psi = 30^\circ$ are not presented because the behaviour was very similar as in Fig. 8. Also, no curve is presented for the profile evolution under densification or expansion with coordination $Z \neq 6$ because the observations are similar whatever Z .

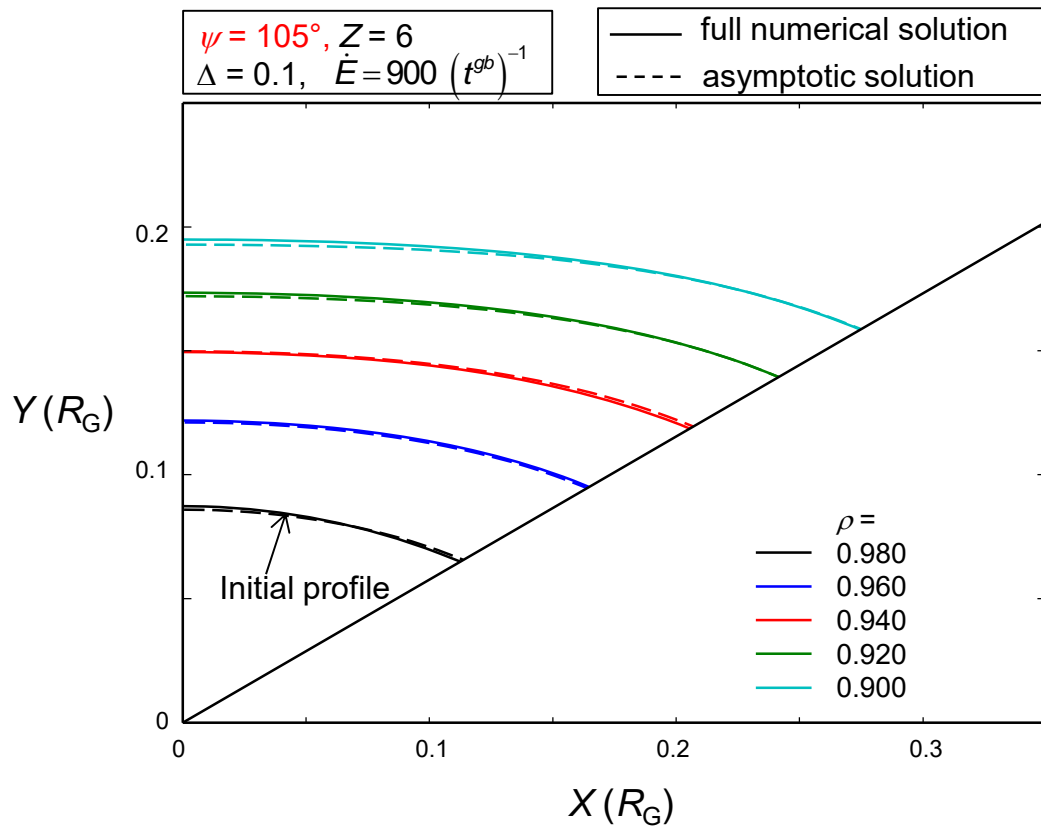


Figure 8: Evolution of pore profiles for $\psi = 105^\circ$ during expansion at $\dot{E} = 900 (t^{gb})^{-1}$ with $\Delta = 0.1$ and $Z = 6$. Initial density is $\rho = 0.980$. The initial profile is the static equilibrium arc of circle. Asymptotic profiles (dashed curves) calculated according to Eq. (A2.16) are compared to the exact profiles (full curves) calculated by the finite difference method.

From the results presented in Figs. 4 to 7, the evolution as a function of ρ of the departure between the full numerical solution of the profile and the asymptotic profile was quantified via the function

$$e(\rho) = \frac{1}{N} \sqrt{\sum_N [Y_{num}(X) - Y_{asympt}(X)]^2} \quad (72)$$

where $Y_{num}(X)$ and $Y_{asympt}(X)$ are the ordinates of the exact and asymptotic profiles, respectively, and N is the number of intervals in the finite difference computation procedure. The points in Fig. 9 present, on semi-logarithmic scales, the evolution of $e(\rho)$ during densification. Computational parameters for the points on graphs 9a, 9b, 9c, and 9d are the same as for the curves in Figs. 4, 5, 6, and 7, respectively (for the expansion case in Fig. 8, $e(\rho)$ remains too small as to allow significant measurement of a damping rate). Fig. 9 shows that, overall, the damping rate increases when ρ increases and decreases when ψ decreases.

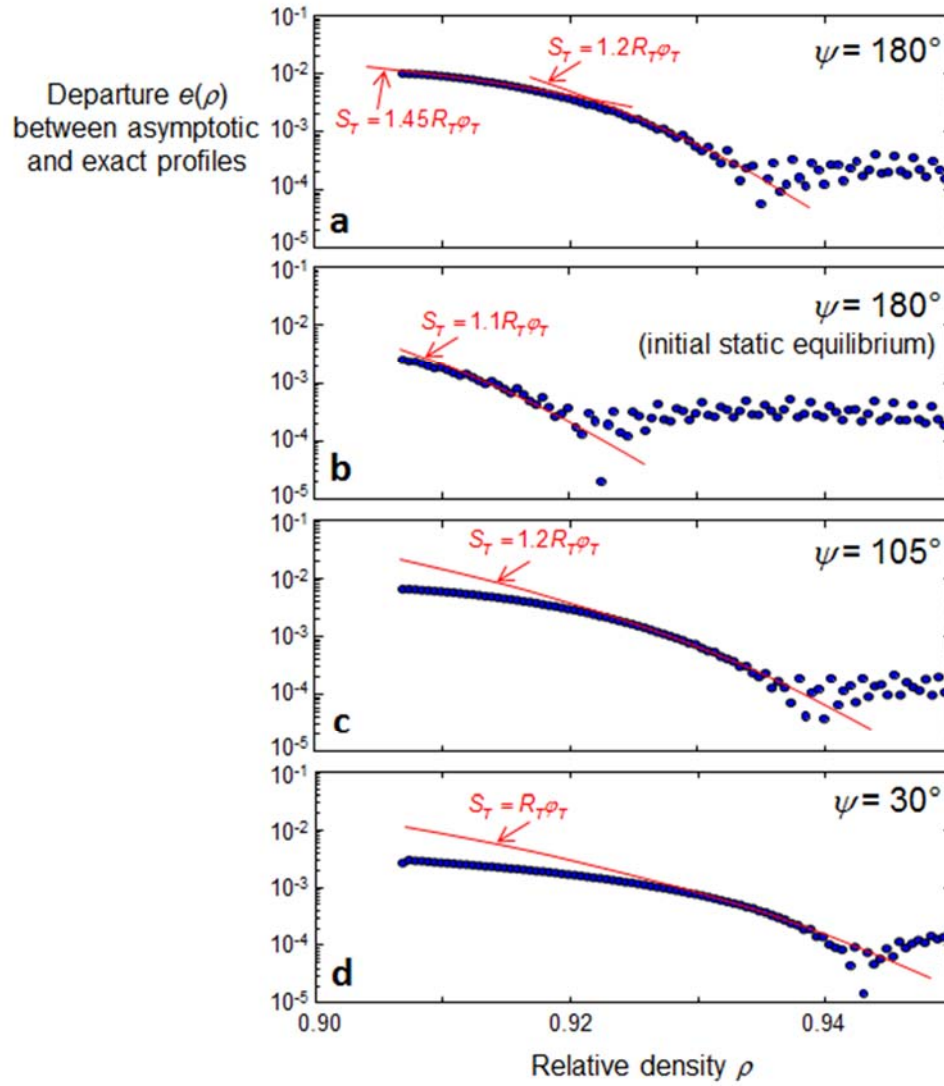


Figure 9 : Departure $e(\rho)$ between full numerical profiles and asymptotic profiles during densification. Computational parameters in a, b, c, and d are the same as in Figs. 4, 5, 6, and 7, respectively. The red curves derive from Eq. (75) using the indicated values for f_0 .

The damping kinetics shown in Fig. 9 can be analysed by assuming that the damping rate of $e(\rho)$ is the same as the damping rate of $[\alpha(\varphi) - \varphi]$ (Eq. (70)). $e(\rho)$ may be expressed in the form

$$e(\rho) = e(\rho_0) e^{-(u(\rho) - u(\rho_0))} \quad (73)$$

where ρ_0 is any particular density and $u(\rho)$ is a function of ρ , and. Accounting for Eqs. (4) and (73), it follows from Eq. (70) that

$$\begin{aligned}
\frac{1}{e(\rho)} \frac{\partial e(\rho)}{\partial \rho} &= - \frac{\partial u(\rho)}{\partial \rho} \\
&\cong \frac{\pi^2}{2\Delta} \frac{Z^2}{(f\varphi_T)^4} \left(\varphi_T - \frac{\cos(\varphi_T + \beta) \sin \varphi_T}{\cos \beta} \right)^2 \frac{1}{t^{gb}} \frac{1}{\dot{E}} \frac{\rho}{(1-\rho)^2}
\end{aligned} \tag{74}$$

Neglecting the dependence of φ_T on ρ , integration of Eq. (75) yields the variation of $e(\rho)$ around density ρ_0 as

$$e(\rho) = e(\rho_0) \exp \left\{ \begin{aligned} &\frac{\pi^2}{2\Delta} \frac{Z^2}{(f_0\varphi_T)^4} \left(\varphi_T - \frac{\cos(\varphi_T + \beta) \sin \varphi_T}{\cos \beta} \right)^2 \\ &\frac{1}{t^{gb}} \frac{1}{\dot{E}} \left[\frac{1}{1-\rho} - \frac{1}{1-\rho_0} + \ln \frac{1-\rho}{1-\rho_0} \right] \end{aligned} \right\} \tag{75}$$

where f_0 is the value of the correction factor f at $\rho = \rho_0$ (Eq. (69)). The red curves in Fig. 9 are drawn around particular ρ_0 values using Eq. (75) with the f_0 factor chosen empirically in such a way as to provide good correspondence with the slope of numerical points around ρ_0 . The purpose of these curves is to show that the kinetics of damping of the transient component of the profile agrees with Eq. (75) provided the correction factor f_0 decreases in the range $1.5 \geq f_0 \geq 1$ when the profile evolves from its initial shape to its asymptotic shape. Qualitatively, this range of evolution of f_0 appears consistent with the shape of the curves in Figs. 4 to 7.

3.2. Dominance of transient or asymptotic behaviours

While the rate of damping of the transient component is given by Eq. (70), the rate of change of the asymptotic profile expresses, according to Eq. (A1.11), as

$$\frac{\dot{R}}{R} \cong \frac{\dot{R}_T}{R_T} = \frac{\xi_T}{\xi^*} \frac{1}{1-\rho} \dot{E} \tag{76}$$

The existence of an asymptotic solution of PDE Eq. (45) is meaningful only if the transient

component of the full solution fades away with time. By analogy with the concept of rate-limiting step in kinetics, we can consider that, at any moment of the sintering process, the evolution of the system is dominated by the phenomenon that evolves at the slowest rate. According to this criterion, from Eqs (70) and (76), the asymptotic, strain-rate-controlled behaviour is dominant if

$$\|\dot{E}\|_{\Delta} < \pi^2 \frac{Z^2}{(f\varphi)^4} \frac{\xi^*}{\xi_T} \left(\varphi_T - \frac{\cos(\varphi_T + \beta) \sin \varphi_T}{\cos \beta} \right)^2 \frac{\rho^2}{1-\rho} \frac{1}{t^{gb}} \quad (77)$$

There thus exists an upper limit of the product $\|\dot{E}\|_{\Delta}$ beyond which the concept of sintering viscosity as a material property is meaningless because the evolution of the system is then dominated by transient phenomena which are not solely linked to strain rate.

Fig.10 presents maps for the variation, in the relative density range $0.6 \geq \rho \geq 1$, of the criterion expressed by Eq. (77) using, as approximations, $\varphi_T = \varphi_{Te}$ and $f = 1$ (Fig. 9 suggests that f becomes close to 1 when approaching the asymptotic regime). The curves are drawn for dihedral angles $\psi = 180^\circ$, 105° , and 30° with grain coordination $Z = 6$. These three ψ values correspond to either convex pores ($\psi = 180^\circ$ and 105°) or concave pores ($\psi = 30^\circ$). The asymptotic behaviour is dominant (i.e. the concept of sintering viscosity is meaningful) only in the part of the map below the curves. The boundary curves increase strongly when relative density increases and when ψ decreases. This results from the fact that the rate of damping of the transient solution increases as the fourth power of the length S_T of the pore profile (Eqs. (69) and (70)): at constant ψ , S_T decreases when ρ increases whereas, at constant ρ , S_T increases when ψ decreases. Fig. 10 allows verifying that, with $Z = 6$ and $\psi = 180^\circ$, 105° , and

30°, the value $\|\dot{E}\|\Delta = -135$ considered for computing the curves of Figs 5 to 8 in the relative density range $0.91 \geq \rho \geq 98$ lies inside the region of dominance of the asymptotic behaviour.

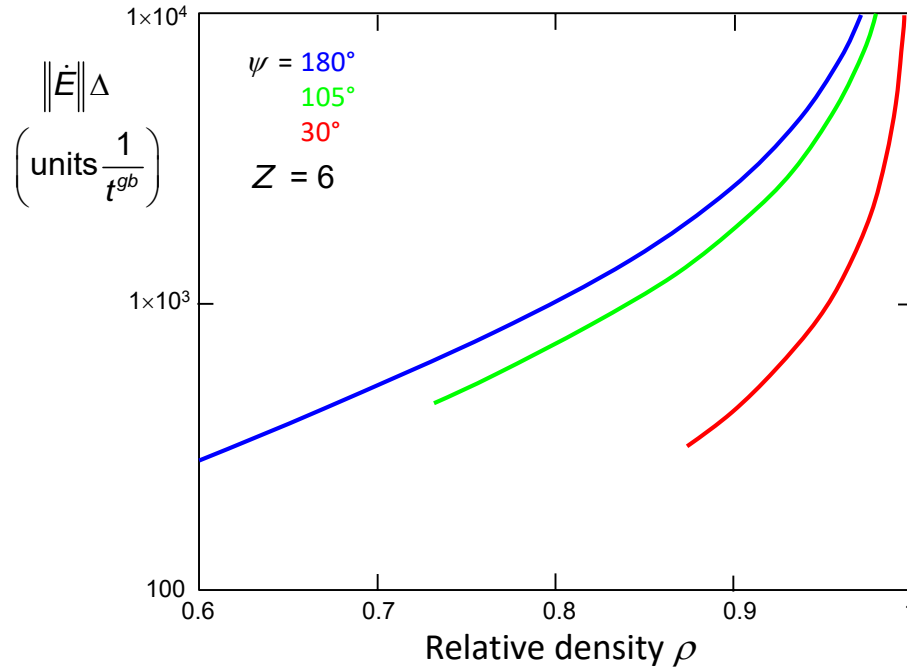


Figure 10: Variation of the criterion expressed by Eq. (77) for $Z = 6$ and $\psi = 180^\circ$, 105° , and 30°

In real aggregates, coordination is low when grains initially get into contact and it increases when density increases. In order to be realistic, computations should account for this dependence of Z on ρ . Only empirical laws have been proposed for describing this dependence in 3D [34]. For the 2D case, we will make use of the phenomenological law represented by the red curve in Fig.11. This law complies with the fact that, in 2D, Z tends to 6 at full density. The blue curve represents the function

$$\rho = \frac{\pi}{Z \tan\left(\frac{\pi}{Z}\right)} \quad (78)$$

which traces the dependence on Z of the relative density at which perfect cylinders with equal diameter would just touch one another (Eq. (78) can be derived by considering the triangular

RVE of Fig. 3). The fact that the curve of Eq. (78) lies above the curve of dependence of Z on ρ is consistent with the progressive growth of grain boundaries during densification.

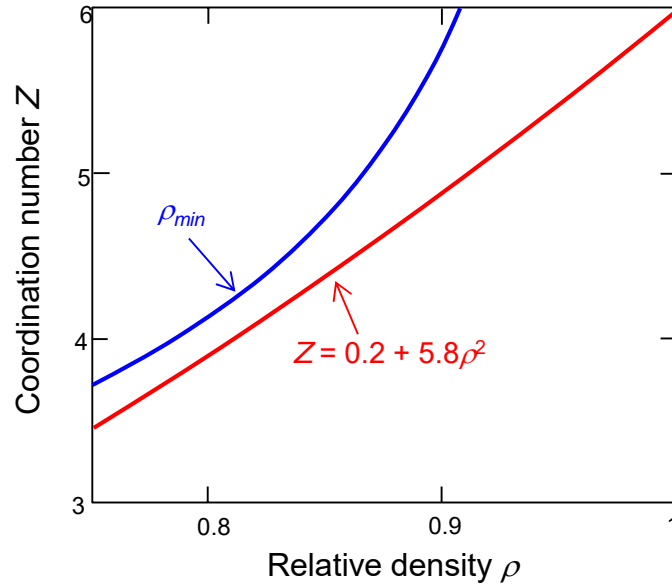


Figure 11: The red curve is the empirical law that is proposed for the variation of Z with ρ in a 2D random array of grains. The blue curve is the dependence on Z of the relative density at which cylinders with equal diameter would just touch one another.

Fig.12 presents maps for the variation of the boundary expressed by Eq. (77) in the relative density range $0.75 \geq \rho \geq 1$ for the same dihedral angles as in Fig.10 but with grain coordination evolving according to the red curve in Fig.11. At the same relative density, the curves are a little lower in Fig.12 than in Fig.10 because a decrease of Z at given ρ causes an increase of the profile length S_T .

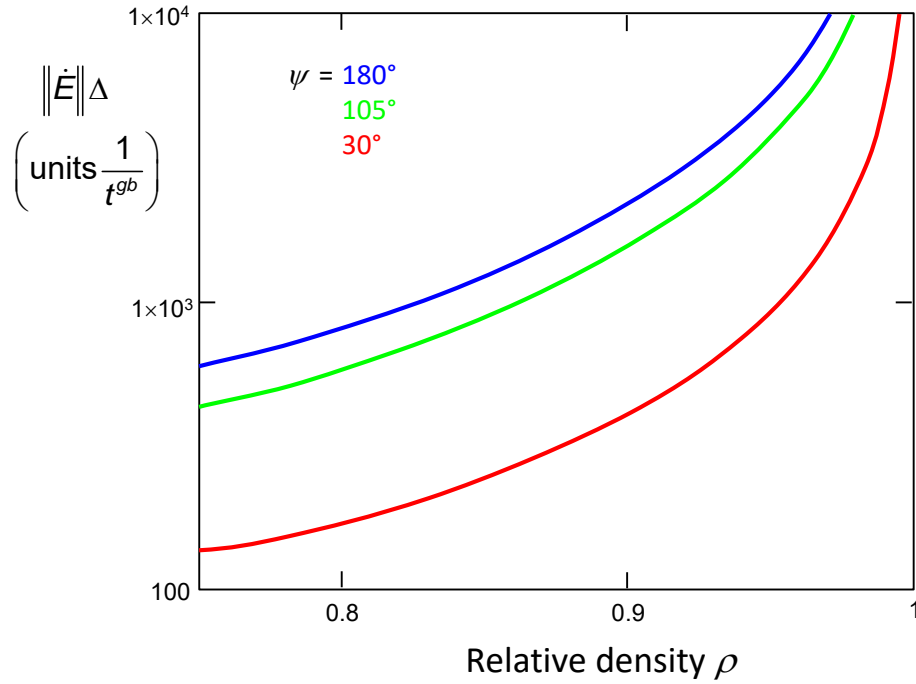


Figure 12 : Variation of the criterion expressed by Eq. (77) for $\psi = 180^\circ$, 105° , and 30° using the

$Z(\rho)$ law represented by the red curve in Fig. 11

3.3. Example of application in sintering simulation

As mentioned in the Introduction, previous models for computing bulk viscosity in sintering rely on the quasi-equilibrium approximation, which neglects the contribution of surface diffusion.

In Ref. [31], the mathematical procedure developed in the present paper is exploited for

unravelling the contribution of surface diffusion to bulk sintering viscosity under high rates of

densification or expansion. It is shown that the ratio $\frac{K}{K_{qe}}$ of the bulk viscosity K (involving the

effect of pore surface diffusion) to the quasi-equilibrium estimate K_{qe} can be written

$$\frac{K}{K_{qe}} = \left[\frac{3}{2} \frac{1}{\dot{E} t^{gb}} \frac{R_G}{H} (B_T K_T - B_{Te} K_e) + \frac{1}{R_G^3} (B_T^3 - B_{Te}^3) \right] \left(\frac{R_G}{B_{Te}} \right)^3 \quad (79)$$

The symbols in Eq. (79) have been defined in the present paper (Fig. 3) and their asymptotic value can be computed using the procedure summarized at the end of Section 2.3.2. The first term between the brackets expresses the additional dissipation arising from diffusion fluxes at pore surface whereas the second term expresses the change of grain boundary dissipation linked to the change of grain boundary size. Fig. 13 presents an illustration of the variation of $\frac{K}{K_{qe}}$ with relative density: the curves show that K_{qe} underestimates K by an amount that drastically increases when relative density decreases and when dihedral angle decreases. It is shown in Ref. [31] that the error can exceed 100% for high values of Δ and \dot{E} .

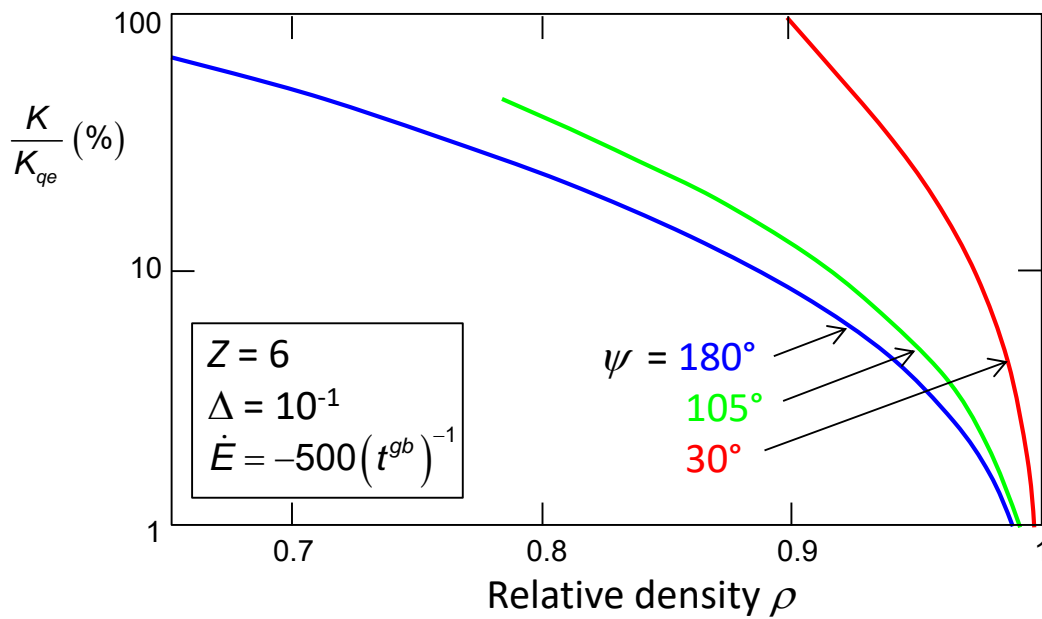


Figure 13 : Ratio of bulk viscosity K (accounting for pore surface diffusion) to K_{qe} (calculated according to the quasi-equilibrium approximation) for three dihedral angles with $Z = 6$, $\Delta = 0.1$,

$$\text{and } \dot{E} = -500(t^{gb})^{-1}.$$

4. Conclusion

When the quasi-equilibrium approximation does not apply, simulation of pore surface evolution during sintering involves accounting for two simultaneous contributions to mass transfer: transient surface diffusion, which is governed by short range curvature gradients, and coupled diffusion at surface and grain boundary, which is governed by strain-rate. The latter contribution dominates during the asymptotic stage of the evolution of the system. Separate identification of these two contributions is a condition for modelling macroscopic viscosity parameters. For this purpose, a mathematical method has been developed in 2D. It has been shown that, via the choice of a properly designed polar coordinate system, the asymptotic solution of the general PDE of the problem can be obtained as the solution of an ODE of which the resolution lends itself to a semi-analytical resolution procedure. The approach also provides an estimate of the rate of convergence of the general solution towards the asymptotic solution. The accuracy of the whole mathematical procedure has been assessed by comparing the evolution of asymptotic and exact profiles under imposed densification or expansion rates. It follows a criterion for delineating, on a map of strain rate versus relative density, the region in which the existence of an asymptotic regime is meaningful. The monotonous dependence of average coordination on relative density can also be taken into account. In Ref. [31], the mathematical procedure developed in the present paper is used for computing the contributions of surface diffusion and grain boundary diffusion to macroscopic bulk viscosity.

5. Data accessibility

This work does not involve external supporting data. All equations and numerical procedures necessary for reproducing the results are provided in the paper.

6. Competing interests

The authors have no competing interests.

7. Author's contributions.

FD conceived the conceptual framework, developed the semi-analytical resolution procedure and interpreted the results. LB developed the finite difference procedure. FD and LB wrote the paper together.

8. Funding and acknowledgements

This work did not rely on particular research funding contract of the authors.

9. Ethics

This work did not involve human subjects, animals, or conservation issues.

Appendix 1: Factor $\left(a + \frac{\dot{H}}{\dot{R}_T}\right)$ in Eq. (54)

As $\alpha_T = \frac{\psi}{2} - \beta$ does not depend on time, we can write, using Eqs. (35) and (38)

$$\begin{aligned}\dot{\phi}_T &= \dot{\alpha}_T + \dot{\zeta}_T = \dot{\zeta}_T \\ &= \frac{1}{1 + \left(\frac{R'}{R}\right)_T^2} \frac{d}{dt} \left(\frac{R'}{R} \right)_T \\ &= - \frac{1}{1 + \left(\frac{R'}{R}\right)_T^2} \left[\frac{\dot{R}_T}{R_T} \left(\frac{R'}{R} \right)_T - \frac{1}{R_T} \left[\frac{\partial}{\partial \phi} \left(\frac{\partial R}{\partial t} \right) \right]_T \right]\end{aligned}\tag{A1.1}$$

For the asymptotic solution $\frac{\partial}{\partial \phi} \left(\frac{\partial R}{\partial t} \right) = 0$. Hence

$$\begin{aligned}\dot{\phi}_T &= - \frac{1}{1 + \tan^2 \zeta_T} \frac{\dot{R}_T}{R_T} \tan \zeta_T \\ &= - \frac{\dot{R}_T}{R_T} \cos \zeta_T \sin \zeta_T \\ &= - \frac{\dot{R}_T}{R_T} \frac{1}{2} \sin [2(\varphi_T - \varphi_{Te})]\end{aligned}\tag{A1.2}$$

and Eq. (42) becomes

$$a = \cos(\varphi_T + \beta) + \frac{1}{2} \sin [2(\varphi_T - \varphi_{Te})] \sin(\varphi_T + \beta)\tag{A1.3}$$

From Eqs. (2) and (29)

$$\frac{1}{1 - \rho} = \frac{1}{\xi_T} \frac{\pi}{Z \tan \beta} \left(\frac{R_G}{R_T} \right)^2 + 1\tag{A1.4}$$

$$\text{Hence } \frac{\dot{\rho}}{(1 - \rho)^2} = - \frac{\rho}{1 - \rho} \left[\frac{\dot{\xi}_T}{\xi_T} + 2 \frac{\dot{R}_T}{R_T} \right]\tag{A1.5}$$

which, using Eq. (4), yields

$$\dot{E} = \frac{\dot{H}}{H} = \frac{1}{2} \left(\frac{R_T}{H} \right)^2 \left[\dot{\xi}_T + 2\xi_T \frac{\dot{R}_T}{R_T} \right] \quad (\text{A1.6})$$

As, from Eqs. (30) and (A1.2)

$$\begin{aligned} \dot{\xi}_T &= \frac{\dot{\varphi}_T}{\tan \beta} \left(1 - \frac{1}{\cos \beta} [\cos(\varphi_T + \beta) \cos \varphi_T - \sin(\varphi_T + \beta) \sin \varphi_T] \right) \\ &= -\frac{\dot{R}_T}{R_T} \frac{1}{2 \tan \beta} \sin[2(\varphi_T - \varphi_{Te})] \left(1 - \frac{\cos(\varphi_T + \beta) \cos \varphi_T - \sin(\varphi_T + \beta) \sin \varphi_T}{\cos \beta} \right) \end{aligned} \quad (\text{A1.7})$$

(A1.6) becomes

$$\dot{E} = \left(\frac{R_T}{H} \right)^2 \frac{\dot{R}_T}{R_T} \left[\xi_T - \frac{1}{4 \tan \beta} \sin[2(\varphi_T - \varphi_{Te})] \left(1 - \frac{\cos(\varphi_T + \beta) \cos \varphi_T - \sin(\varphi_T + \beta) \sin \varphi_T}{\cos \beta} \right) \right] \quad (\text{A1.8})$$

One thus obtains via Eqs. (3) and (29)

$$\frac{\dot{H}}{\dot{R}_T} = \xi^* \frac{R_T}{H} = \pm \xi^* \sqrt{\frac{1-\rho}{\xi_T}} \quad (\text{A1.9})$$

with

$$\xi^* = \xi_T - \frac{1}{4 \tan \beta} \sin[2(\varphi_T - \varphi_{Te})] \left(1 - \frac{\cos(\varphi_T + \beta) \cos \varphi_T - \sin(\varphi_T + \beta) \sin \varphi_T}{\cos \beta} \right) \quad (\text{A1.10})$$

In (A1.9), the plus sign holds for convex pores and the minus sign for concave pores. Eq. (A1.6) yields alternatively,

$$\begin{aligned} \frac{\dot{R}_T}{R_T} &= \frac{1}{\xi^*} \left(\frac{H}{R_T} \right)^2 \frac{\dot{H}}{H} \\ &= \frac{\xi_T}{\xi^*} \frac{1}{1-\rho} \dot{E} \end{aligned} \quad (\text{A1.11})$$

Appendix 2: Analytical resolution of asymptotic ODE (Eq. (54))

The resolution procedure involves five steps.

A2.1. Diffusion flux j_s

According to Eq. (16)

$$V_{diff} = \Omega \frac{\partial j_s}{\partial S} = -\frac{1}{\Delta} \frac{\delta D_{gb} \gamma_s \Omega}{kT} \frac{\partial^2 \kappa}{\partial S^2} \quad (\text{A2.1})$$

j_s is thus obtained by integrating Eq. (54):

$$j_s = -\frac{1}{\Omega} \dot{R}_T \int_0^S \frac{1}{\cos \zeta} (b - c \cos \varphi) dS \quad (\text{A2.2})$$

with $b = \frac{\dot{R}_\infty}{\dot{R}_T}$ (A2.3)

and $c = \frac{1}{\cos \beta} \left(a + \xi^* \frac{R_T}{H} \right)$ (A2.4)

$$= \frac{1}{\cos \beta} \left(a \pm \xi^* \sqrt{\frac{1-\rho}{\xi_T}} \right)$$

where ξ_T , a , and ξ^* are given by Eqs. (30), (A1.3), and (A1.10), respectively. Eq. (A2.2) can be integrated analytically if one adopts the approximations (57) and

$$\frac{dS}{\cos \zeta} = R d\varphi \frac{1}{(\cos \zeta)^2} \cong R_T d\varphi \quad (\text{A2.5}).$$

Using Eqs. (A1.9) and (A1.11), the integration yields

$$j_s \cong -\frac{1}{\Omega} \frac{1}{\xi^*} H \dot{H} (b\varphi - c \sin \varphi) = -\frac{1}{\Omega} \dot{E} \frac{1}{1-\rho} \frac{\xi_T}{\xi^*} R_T^2 (b\varphi - c \sin \varphi) \quad (\text{A2.6})$$

The integration constant is null owing to boundary condition (51). Via Eq. (31), boundary condition (52) writes

$$\begin{aligned}
-\frac{1}{\Omega} \frac{1}{\xi^*} H \dot{H} \left[b \varphi_T - \frac{1}{\cos \beta} \left(a + \xi^* \frac{R_T}{H} \right) \sin \varphi_T \right] &= -\frac{1}{\Omega} B_T \dot{H} \\
&= -\frac{1}{\Omega} \dot{H} \left(H \tan \beta - R_T \frac{\sin \varphi_T}{\cos \beta} \right)
\end{aligned} \tag{A2.7}$$

Using Eq. (A1.10), (A2.7) yields the identification of b merely as $b = 1$, i.e.

$$\dot{R}_\infty = \dot{R}_T \tag{A2.8}$$

A2.2. Curvature κ

According to Eq. (A2.1), pore surface curvature κ is obtained by integrating Eq. (A2.6):

$$\frac{d\kappa}{R_T d\varphi} = \Delta \frac{t^{gb}}{R_G^4} \dot{E} \frac{1}{1-\rho} \frac{\xi_T}{\xi^*} R_T^2 [\varphi - c \sin \varphi] \tag{A2.9}$$

where use has been made of Eq. (71) for the definition of t^{gb} . Hence

$$\kappa = \Delta \frac{t^{gb}}{R_G^4} \dot{E} \frac{1}{u} \frac{\xi_T}{\xi^*} R_T^3 \left(\frac{1}{2} \varphi^2 + c \cos \varphi \right) + Cst_1 \tag{A2.10}$$

A2.3. Slope of pore profile α

In turn, α , is obtained from Eq. (59):

$$\kappa = \frac{d\alpha}{dS} \cong \frac{1}{R_T} \frac{d\alpha}{d\varphi}$$

$$\text{i.e.} \quad \alpha = \Delta \frac{t^{gb}}{R_G^4} \dot{E} \frac{1}{1-\rho} \frac{\xi_T}{\xi^*} R_T^4 \left(\frac{1}{6} \varphi^3 + c \sin \varphi \right) + \varphi R_T Cst_1 + Cst_2 \tag{A2.11}$$

Boundary condition (49) brings $Cst_2 = 0$ whereas boundary condition (50) brings

$$Cst_1 = \frac{1}{R_T} \frac{\varphi_{Te}}{\varphi_T} - \Delta \frac{t^{gb}}{R_G^4} \frac{\dot{E}}{1-\rho} \frac{\xi_T}{\xi^*} R_T^3 \left(\frac{1}{6} \varphi_T^2 + c \frac{\sin \varphi_T}{\varphi_T} \right) \tag{A2.12}$$

Thus, Eq. (A2.12) becomes

$$\alpha = \varphi \left(\frac{\varphi_{Te}}{\varphi_T} - \Delta \frac{t^{gb}}{R_G^4} \frac{\dot{E}}{1-\rho} \frac{\xi_T}{\xi^*} R_T^4 \left(\frac{1}{6} \varphi_T^2 + c \frac{\sin \varphi_T}{\varphi_T} \right) \right) + \Delta \frac{t^{gb}}{R_G^4} \frac{\dot{E}}{1-\rho} \frac{\xi_T}{\xi^*} R_T^4 \left(\frac{1}{6} \varphi^3 + c \sin \varphi \right) \quad (A2.13)$$

and, from Eqs (2) and (A2.10), surface curvature at T is

$$\kappa_T = \frac{1}{R_T} \frac{\varphi_{Te}}{\varphi_T} + t^{gb} \dot{E} \Delta \frac{1}{R_T} \frac{1-\rho}{\rho^2} \left(\frac{\pi}{Z \tan \beta} \right)^2 \frac{1}{\xi_T} \frac{1}{\xi^*} \left(\frac{1}{3} \varphi_T^2 + c \left(\cos \varphi_T - \frac{\sin \varphi_T}{\varphi_T} \right) \right) \quad (A2.14)$$

A2.4. Radial coordinate R

From Eqs. (34), (35) and (A2.5),

$$\begin{aligned} \zeta &= \varphi - \alpha \\ &\cong \frac{1}{R} \frac{dR}{d\varphi} \\ &\cong \frac{1}{R_T} \frac{dR}{d\varphi} \end{aligned} \quad (A2.15)$$

Hence

$$\begin{aligned} \frac{R}{R_T} - 1 &= \int_{\varphi_T}^{\varphi} (\varphi - \alpha) d\varphi \\ &= \int_{\varphi_T}^{\varphi} \left[\varphi \left(1 - \frac{\varphi_{Te}}{\varphi_T} + \Delta \frac{t^{gb}}{R_G^4} \frac{\dot{E}}{1-\rho} \frac{\xi_T}{\xi^*} R_T^3 \left(\frac{1}{6} \varphi_T^2 + c \frac{\sin \varphi_T}{\varphi_T} \right) \right) - \Delta \frac{t^{gb}}{R_G^4} \frac{\dot{E}}{1-\rho} \frac{\xi_T}{\xi^*} R_T^3 \left(\frac{1}{6} \varphi^3 + c \sin \varphi \right) \right] d\varphi \quad (A2.16) \\ &= \frac{1}{2} (\varphi^2 - \varphi_T^2) \left(1 - \frac{\varphi_{Te}}{\varphi_T} + \Delta \frac{t^{gb}}{R_G^4} \frac{\dot{E}}{1-\rho} \frac{\xi_T}{\xi^*} R_T^4 \left(\frac{1}{6} \varphi_T^2 + c \frac{\sin \varphi_T}{\varphi_T} \right) \right) \\ &\quad - \Delta \frac{t^{gb}}{R_G^4} \frac{\dot{E}}{1-\rho} \frac{\xi_T}{\xi^*} R_T^4 \left(\frac{1}{24} (\varphi^4 - \varphi_T^4) - c (\cos \varphi - \cos \varphi_T) \right) \end{aligned}$$

A2.5. $\varphi_{Te} - \varphi_T$

Using Eq. (A2.5), relative density writes, according to Eqs. (29) and (30)

$$\begin{aligned}
 1 - \rho &= \frac{1}{H^2 \tan \beta} \left(\int_0^{S_T} R \cos \zeta dS - R_T^2 \frac{\cos(\varphi_T + \beta)}{\cos \beta} \sin \varphi_T \right) \\
 &= \frac{1}{H^2 \tan \beta} \left(\int_0^{S_T} R R_T d\varphi - R_T^2 \frac{\cos(\varphi_T + \beta)}{\cos \beta} \sin \varphi_T \right) \\
 &= \frac{R_T^2}{H^2 \tan \beta} \left(\int_0^{\varphi_T} \frac{R}{R_T} d\varphi - \frac{\cos(\varphi_T + \beta)}{\cos \beta} \sin \varphi_T \right) \\
 &= \frac{R_T^2}{H^2 \tan \beta} \left(\varphi_T - \frac{\cos(\varphi_T + \beta)}{\cos \beta} \sin \varphi_T \right)
 \end{aligned} \tag{A2.17}$$

This implies

$$\int_0^{\varphi_T} \frac{R}{R_T} d\varphi = \varphi_T \tag{A2.18}$$

From Eq. (A2.16)

$$\begin{aligned}
 \int_0^{\varphi_T} \frac{R}{R_T} d\varphi &= \int_0^{\varphi_T} \left(1 + \frac{1}{2} (\varphi^2 - \varphi_T^2) \left(1 - \frac{\varphi_{Te}}{\varphi_T} + \Delta \frac{t^{gb}}{R_G^4} \frac{\dot{E}}{1-\rho} \frac{\xi_T}{\xi^*} R_T^4 \left(\frac{1}{6} \varphi_T^2 + c \frac{\sin \varphi_T}{\varphi_T} \right) \right) \right. \\
 &\quad \left. - \Delta \frac{t^{gb}}{R_G^4} \frac{\dot{E}}{1-\rho} \frac{\xi_T}{\xi^*} R_T^4 \left(\frac{1}{24} (\varphi^4 - \varphi_T^4) - c (\cos \varphi - \cos \varphi_T) \right) \right) d\varphi \tag{A2.19} \\
 &= \varphi_T - \frac{1}{3} \varphi_T^3 \left(1 - \frac{\varphi_{Te}}{\varphi_T} \right) - \Delta \frac{t^{gb}}{R_G^4} \frac{\dot{E}}{1-\rho} \frac{\xi_T}{\xi^*} R_T^4 \left[\frac{4}{180} \varphi_T^5 + c \left(\sin \varphi_T \left(\frac{1}{3} \varphi_T^2 - 1 \right) + \varphi_T \cos \varphi_T \right) \right]
 \end{aligned}$$

Using Eq. (2), one obtains finally

$$\begin{aligned}
 \varphi_{Te} - \varphi_T &= \Delta \frac{t^{gb}}{R_G^4} \frac{\dot{E}}{1-\rho} \frac{\xi_T}{\xi^*} R_T^4 \frac{3}{\varphi_T^2} \left[\frac{4}{180} \varphi_T^5 + c \left(\sin \varphi_T \left(\frac{1}{3} \varphi_T^2 - 1 \right) + \varphi_T \cos \varphi_T \right) \right] \\
 &= t^{gb} \dot{E} \Delta \frac{1-\rho}{\rho^2} \left(\frac{\pi}{Z \tan \beta} \right)^2 \frac{1}{\xi_T} \frac{1}{\xi^*} \left[\frac{1}{15} \varphi_T^3 + c \left(\sin \varphi_T \left(1 - \frac{3}{\varphi_T^2} \right) + 3 \frac{\cos \varphi_T}{\varphi_T} \right) \right]
 \end{aligned} \tag{A2.20}.$$

References

- [1] Nichols, F. & Mullins, W. 1965 Surface- and volume-diffusion contributions to morphological changes driven by capillarity *AIME Met Soc Trans* **233**, 1840-1848. (doi:10.1063/1.1714360).
- [2] Coble, R. 1958 Initial sintering of alumina and hematite. *Journal of the American Ceramic Society* **41**, 55-62. (doi:10.1111/j.1151-2916.1958.tb13519.x).
- [3] Coble, R.L. 1961 Sintering crystalline solids. II. Experimental test of diffusion models in powder compacts. *J Appl Phys* **32**, 793-799. (doi:10.1063/1.1736108).
- [4] Jagota, A., Mikeska, K.R. & Bordia, R.K. 1990 Isotropic constitutive model for sintering particle packings. *Journal of the American Ceramic Society* **73**, 2266-2273. (doi:10.1111/j.1151-2916.1990.tb07587.x).
- [5] McMeeking, R. & Kuhn, L. 1992 A diffusional creep law for powder compacts. *Acta metallurgica et materialia* **40**, 961-969. (doi:10.1016/0956-7151(92)90073-N).
- [6] Riedel, H., Zipse, H. & Svoboda, J. 1994 Equilibrium pore surfaces, sintering stresses and constitutive equations for the intermediate and late stages of sintering—II. Diffusional densification and creep. *Acta metallurgica et materialia* **42**, 445-452. (doi:10.1016/0956-7151(94)90499-5).
- [7] Wakai, F. & Akatsu, T. 2010 Anisotropic viscosities and shrinkage rates in sintering of particles arranged in a simple orthorhombic structure. *Acta Materialia* **58**, 1921-1929. (doi:10.1016/j.actamat.2009.11.035).
- [8] Wakai, F. & Nikolić, Z.S. 2011 Effect of grain boundary sliding on shear viscosity and viscous Poisson's ratio in macroscopic shrinkage during sintering. *Acta Materialia* **59**, 774-784. (doi:10.1016/j.actamat.2010.10.021).
- [9] Cocks, A.C., Gill, S.P. & Pan, J. 1998 Modelling microstructure evolution in engineering materials. *Advances in Applied Mechanics* **36**, 81-162. (doi:10.1016/S0065-2156(08)70185-6).
- [10] Li, F., Pan, J., Guillon, O. & Cocks, A. 2010 Predicting sintering deformation of ceramic film constrained by rigid substrate using anisotropic constitutive law. *Acta Materialia* **58**, 5980-5988. (doi:10.1016/j.actamat.2010.07.015).
- [11] Delannay, F. 2015 Sintering Kinetics Across Pore Closure Transition Accounting for Continuous Increase in Grain Coordination with Density. *Journal of the American Ceramic Society* **98**, 3476-3482. (doi:DOI: 10.1111/jace.13594).
- [12] Kraft, T. & Riedel, H. 2002 Numerical simulation of die compaction and sintering. *Powder Metall* **45**, 227-231. (doi:10.1179/003258902225006989).
- [13] Munir, Z., Anselmi-Tamburini, U. & Ohyanagi, M. 2006 The effect of electric field and pressure on the synthesis and consolidation of materials: A review of the spark plasma sintering method. *Journal of Materials Science* **41**, 763-777. (doi:10.1007/s10853-006-6555-2).
- [14] Garay, J. 2010 Current-activated, pressure-assisted densification of materials. *Annual review of materials research* **40**, 445-468. (doi:10.1146/annurev-matsci-070909-104433).
- [15] Cologna, M., Rashkova, B. & Raj, R. 2010 Flash Sintering of Nanograin Zirconia in < 5 s at 850 C. *Journal of the American Ceramic Society* **93**, 3556-3559. (doi:10.1111/j.1551-2916.2010.04089.x).
- [16] Guillon, O., Gonzalez-Julian, J., Dargatz, B., Kessel, T., Schierning, G., Räthel, J. & Herrmann, M. 2014 Field-assisted sintering technology/spark plasma sintering: mechanisms, materials, and technology developments. *Advanced Engineering Materials* **16**, 830-849. (doi:10.1002/adem.201300409).

- [17] Todd, R., Zapata-Solvas, E., Bonilla, R., Sneddon, T. & Wilshaw, P. 2015 Electrical characteristics of flash sintering: thermal runaway of Joule heating. *Journal of the European Ceramic Society* **35**, 1865-1877. (doi:<https://doi.org/10.1016/j.jeurceramsoc.2014.12.022>).
- [18] Wakai, F. & Brakke, K.A. 2011 Mechanics of sintering for coupled grain boundary and surface diffusion. *Acta Materialia* **59**, 5379-5387. (doi:10.1016/j.actamat.2011.05.006).
- [19] Bouvard, D. & McMeeking, R. 1996 Deformation of Interparticle Necks by Diffusion-Controlled Creep. *Journal of the American Ceramic Society* **79**, 666-672.
- [20] Svoboda, J. & Riedel, H. 1995 New solutions describing the formation of interparticle necks in solid-state sintering. *Acta metallurgica et materialia* **43**, 1-10. (doi:10.1016/0956-7151(95)90255-4).
- [21] Zhang, W. & Gladwell, I. 1998 Sintering of two particles by surface and grain boundary diffusion – a three-dimensional model and a numerical study. *Comput Mater Sci* **12**, 84-104.
- [22] Maximenko, A.L. & Olevsy, E.A. 2004 Effective diffusion coefficients in solid-state sintering. *Acta Materialia* **52**, 2953-2963. (doi:10.1016/j.actamat.2004.02.042).
- [23] Hsueh, C. & Evans, A. 1981 Overview 14 Creep fracture in ceramic polycrystals—II. effects of inhomogeneity on creep rupture. *Acta Metallurgica* **29**, 1907-1917. (doi:10.1016/0001-6160(81)90028-6).
- [24] Riedel, H. 1990 A Constitutive Model for the Finite-Element Simulation of Sintering--Distortions and Stresses. *Ceramic Powder Science III*, 619-630.
- [25] Mullins, W. 1993 Idealized two dimensional sintering by interface diffusion. *Scripta metallurgica et materialia* **29**, 491-496. (doi:10.1016/0956-716X(93)90153-J).
- [26] Mullins, W. 1995 Mass transport at interfaces in single component systems. *Metallurgical and Materials Transactions A* **26**, 1917-1929. (doi:10.1007/BF02670663).
- [27] Zhang, W., Schneibel, J.H. & Hsueh, C.-H. 1994 Sintering of regular two-dimensional arrays of particles by surface and grain boundary diffusion. *Philosophical Magazine A* **70**, 1107-1118. (doi:10.1080/01418619408242952).
- [28] Pan, J. & Cocks, A. 1995 A numerical technique for the analysis of coupled surface and grain-boundary diffusion. *Acta metallurgica et materialia* **43**, 1395-1406. (doi:10.1016/0956-7151(94)00365-O).
- [29] Svoboda, J. & Riedel, H. 1995 Quasi-equilibrium sintering for coupled grain-boundary and surface diffusion. *Acta metallurgica et materialia* **43**, 499-506. (doi:10.1016/0956-7151(94)00249-H).
- [30] Subramanian, S. & Sofronis, P. 2001 Modeling the interaction between densification mechanisms in powder compaction. *International journal of solids and structures* **38**, 7899-7918. (doi:10.1016/S0020-7683(01)00096-8).
- [31] Delannay, F. & Brassart, L. 2018 Strain rate dependence of the contribution of surface diffusion to bulk sintering viscosity. *J. American Ceramic Society* (**in press**).
- [32] Suo, Z. 1997 Motions of Microscopic Surfaces. *Solid Mechanics* **33**, 193. (doi:10.1016/S0065-2156(08)70387-9).
- [33] Svoboda, J. & Riedel, H. 1992 Pore-boundary interactions and evolution equations for the porosity and the grain size during sintering. *Acta Metallurgica et Materialia* **40**, 2829-2840. (doi:10.1016/0956-7151(92)90448-N).
- [34] German, R.M. 2014 Coordination number changes during powder densification. *Powder Technology* **253**, 368-376. (doi:10.1016/j.powtec.2013.12.006).

Figures captions

Figure 1: Two types of surface diffusion fluxes: fluxes j_{sA} (red) feed grain boundary diffusion fluxes j_{gb} , the divergence of which brings about relative displacement of the centroids of grains 1 and 2; fluxes j_{sB} (green) are driven by small scale curvature gradient and are not coupled to macroscopic strain rate.

Figure 2: Arrays of identical grains with $Z = 4$ and 6 under radial strain rate \dot{E} . RVEs are triangles in grey shade.

Figure 3 : RVE in the case of convex pore curvature with $\dot{E} < 0$. (a) Dynamic and static profile parameters. (b) Cartesian coordinates X and Y and current coordinate S . (c) Polar coordinates R and φ .

Figure 4: Evolution of pore profiles for $\psi = 180^\circ$ during densification at $\dot{E} = -1350(t^{gb})^{-1}$ with $\Delta = 0.1$ and $Z = 6$. Initial density is $\rho = 0.907$. The initial profile presents a small neck close to particle contact. Asymptotic profiles (dashed curves) calculated according to Eq. (A2.16) are compared to the exact profiles (full curves) calculated via the finite difference method.

Figure 5: Evolution of pore profiles for $\psi = 180^\circ$ during densification at $\dot{E} = -1350(t^{gb})^{-1}$ with $\Delta = 0.1$ and $Z = 6$. Initial density is $\rho = 0.907$. The initial profile is the arc of circle of static equilibrium. Asymptotic profiles (dashed curves) calculated according to Eq. (A2.16) are compared to the exact profiles (full curves) calculated via the finite difference method.

Figure 6: Evolution of pore profiles for $\psi = 105^\circ$ during densification at $\dot{E} = -1350(t^{gb})^{-1}$ with $\Delta = 0.1$ and $Z = 6$. Initial density is $\rho = 0.907$. The initial profile presents a small neck close to particle contact. Asymptotic profiles (dashed curves) calculated according to Eq. (A2.16) are compared to the exact profiles (full curves) calculated via the finite difference method.

Figure 7: Evolution of pore profiles for $\psi = 30^\circ$ during densification at $\dot{E} = -1350(t^{gb})^{-1}$ with $\Delta = 0.1$ and $Z = 6$. Initial density is $\rho = 0.907$. The initial profile presents a small neck close to

particle contact. Asymptotic profiles (dashed curves) calculated according to Eq. (A2.16) are compared to the exact profiles (full curves) calculated via the finite difference method.

Figure 8: Evolution of pore profiles for $\psi = 105^\circ$ during expansion at $\dot{E} = 900(t^{gb})^{-1}$ with $\Delta = 0.1$ and $Z = 6$. Initial density is $\rho = 0.980$. The initial profile is the static equilibrium arc of circle. Asymptotic profiles (dashed curves) calculated according to Eq. (A2.16) are compared to the exact profiles (full curves) calculated by the finite difference method.

Figure 9 : Departure $e(\rho)$ between full numerical profiles and asymptotic profiles during densification. Computational parameters in a, b, c, and d are the same as in Figs. 4, 5, 6, and 7, respectively. The red curves derive from Eq. (75) using the indicated values for f_0 .

Figure 10: Variation of the criterion expressed by Eq. (77) for $Z = 6$ and $\psi = 180^\circ, 105^\circ$, and 30°

Figure 11: The red curve is the empirical law that is proposed for the variation of Z with ρ in a 2D random array of grains. The blue curve is the dependence on Z of the relative density at which cylinders with equal diameter would just touch one another.

Figure 12 : Variation of the criterion expressed by Eq. (77) for $\psi = 180^\circ, 105^\circ$, and 30° using the $Z(\rho)$ law represented by the red curve in Fig. 11

Figure 13 : Ratio of bulk viscosity K (accounting for pore surface diffusion) to K_{qe} (calculated according to the quasi-equilibrium approximation) for three dihedral angles with $Z = 6$, $\Delta = 0.1$, and $\dot{E} = -500(t^{gb})^{-1}$.